Monthly Notices
of the
ROYAL ASTRONOMICAL SOCIETY

MNRAS **494,** 6103–6119 (2020)
Advance Access publication 2020 May 5

doi:10.1093/mnras/staa908

Electric heating and angular momentum transport in laminar models of protoplanetary discs

William Béthune[1]★ and Henrik Latter[2]

[1]*Institut für Astronomie und Astrophysik, Universität Tübingen, Auf der Morgenstelle 10, D-72076 Tübingen, Germany*
[2]*DAMTP, University of Cambridge, CMS, Wilberforce Road, Cambridge CB3 0WA, UK*

Accepted 2020 March 30. Received 2020 March 29; in original form 2020 January 30

ABSTRACT

The vertical temperature structure of a protoplanetary disc bears on several processes relevant to planet formation, such as gas and dust grain chemistry, ice lines, and convection. The temperature profile is controlled by irradiation from the central star and by any internal source of heat such as might arise from gas accretion. We investigate the heat and angular momentum transport generated by the resistive dissipation of magnetic fields in laminar discs. We use local 1D simulations to obtain vertical temperature profiles for typical conditions in the inner disc (0.5–4 au). Using simple assumptions for the gas ionization and opacity, the heating and cooling rates are computed self-consistently in the framework of radiative non-ideal magnetohydrodynamics. We characterize steady solutions that are symmetric about the mid-plane and which may be associated with saturated Hall-shear unstable modes. We also examine the dissipation of electric currents driven by global accretion-ejection structures. In both cases we obtain significant heating for a sufficiently high opacity. Strong magnetic fields can induce an order-unity temperature increase in the disc mid-plane, a convectively unstable entropy profile, and a surface emissivity equivalent to a viscous heating of $\alpha \sim 10^{-2}$. These results show how magnetic fields may drive efficient accretion and heating in weakly ionized discs where turbulence might be inefficient, at least for a range of radii and ages of the disc.

Key words: accretion, accretion discs – MHD – radiation: dynamics – protoplanetary discs.

1 INTRODUCTION

The imaging of dust substructures (ALMA Partnership et al. 2015; Andrews et al. 2018) and measurements of gas kinematics (Flaherty et al. 2015, 2017; Louvet et al. 2018) have provided valuable clues to the long-standing issues of gas accretion and planet formation in circumstellar discs. Of particular relevance for planet formation is the thermal structure of the disc, which is tightly connected to the accretion process.

The temperature distribution determines the radial location of ice lines, with consequences on grain growth (Lorek, Lacerda & Blum 2018), the preferential sites of planet formation (Ida & Lin 2008; Cridland, Pudritz & Birnstiel 2017; Hyodo, Ida & Charnoz 2019) and their composition (Dodson-Robinson et al. 2009; Cridland, Pudritz & Alessi 2016; Bitsch, Raymond & Izidoro 2019). The temperature of the disc controls its chemistry (Walsh, Nomura & van Dishoeck 2015; Kamp et al. 2017), which goes into our interpretation of molecular emission lines (e.g. Flaherty et al. 2015; Oya et al. 2019). Finally, by affecting the ionization state of the gas (Weingartner & Draine 2001; Ilgner 2012), the temperature may also influence how magnetic fields impact on the disc dynamics.

The temperature of the disc results from a balance between stellar irradiation, internal heating mechanisms, and radiative cooling. In the inner regions of protoplanetary discs, heating is dominated by the liberation of gravitational energy through gas accretion (D'Alessio et al. 1998). Magnetic fields are believed to play a major role in the transport of angular momentum responsible for accretion, whether they power magnetized outflows (Pudritz & Norman 1983; Pelletier & Pudritz 1992) or seed turbulence via the magnetorotational instability (MRI, Balbus & Hawley 1991; Hawley & Balbus 1992). However, the details of angular momentum transport and energy dissipation are often concealed in an effective viscosity parameter α (Shakura & Sunyaev 1973). The bulk accretion rates are consistent with $\alpha \sim 10^{-4}$–10^{-2} in young stellar objects (Bell & Lin 1994), but the accretion process might be vertically inhomogeneous (Gammie 1996), and linking α to a vertical temperature profile pre-supposes that the accretion energy is dissipated locally (Balbus & Papaloizou 1999).

When accounting for the low ionization fraction, magnetohydrodynamic (MHD) simulations support a picture of laminar accretion in the inner regions of protoplanetary discs. Angular momentum is transported by a non-turbulent magnetic stress through the disc

★ E-mail: william.bethune@uni-tuebingen.de

(Lesur, Kunz & Fromang 2014; Bai 2015) and by magnetothermal winds out of the disc (Béthune, Lesur & Ferreira 2017; Bai 2017). Given the complex nature of global MHD simulations, only a few studies have incorporated radiative effects (Wang, Bai & Goodman 2019; Rodenkirch et al. 2020) with a focus on the disc–wind interaction. Electric dissipation is predicted to efficiently heat the wind (Safier 1993), but its contribution inside the disc was only recently examined by Mori, Bai & Okuzumi (2019) who concluded that it should be negligible when compared to stellar irradiation. However, the isothermal model of Mori et al. (2019) did not self-consistently solve for the thermal structure of the disc.

We compute the 1D vertical structure of the inner 0.5−4 au in radiative MHD models of protoplanetary discs. Our model improves on previous studies by self-consistently describing the energy exchanges due to Ohmic resistivity, the Hall effect, ambipolar diffusion, and radiative transport for plausible ionization fractions and opacities. A high-order spatial method helps us resolve the sharp current sheets developing in ambipolar MHD (Brandenburg & Zweibel 1994) and our method is free from the constraints of explicit time-integration schemes, allowing us to probe resistivity regimes inaccessible to common simulation codes.

We link the resistive electric heating to the accretion power and characterize them in terms of a gas temperature and an effective 'viscosity' coefficient α. We consider two different drivers of mass accretion/electric currents inside the disc. In the first case, electric currents are amplified by the Hall-shear instability (HSI, Kunz 2008) and we examine the 1D saturated phase of this instability. Because the instability extracts orbital energy from inside the disc, we designate these solutions as *internally driven*. In the second case, we impose the total electric current passing through the disc and let the current density find the path of least resistance. This situation mimics magnetized accretion-ejection for which a proper energy budget would involve the entire disc-wind system. Since we focus on the internal structure of the disc only, the accretion power appears to be *externally driven*.

In both cases, the resistive dissipation of electric currents can generate as much heat as viscous discs models with $\alpha \sim 10^{-4}$–10^{-2}, and correspondingly large-mass accretion rates. If the disc is opaque at thermal wavelengths, this heat can build-up in the mid-plane and dominate over stellar irradiation in the thermal balance of the disc.

We present our disc model and the system of radiative MHD equations describing it in Section 2. We also detail the theoretical framework in which our results can be interpreted. The results are split into two sections depending on the origin of the accretion power: we present internally driven solutions in Section 3 and externally driven solutions in Section 4. We interpret these results and discuss the limitations of our model in Section 5 before concluding.

2 METHOD

The thermal structure of a passive disc is solely governed by the stellar irradiation, its reprocessing and re-emission at thermal wavelengths. The dissipation of electric currents introduces an additional source of heat in magnetized discs. We aim to compute the vertical structure of axisymmetric protoplanetary discs threaded by a net poloidal magnetic field, irradiated by the central star, and subject to such non-ideal MHD processes.

We consider quasi-equilibrium structures whose relaxation times are short compared to the long-time and large-scale evolution of the disc via mass losses, magnetic flux transport, and the disc's changing radiative environment. We also assume that at any given disc radius, the main physics determining these states is independent of neighbouring radial annuli. Given these restrictions, the most natural framework is the stratified shearing box whose input parameters (irradiation flux, surface density, etc.) depend on radius according to a pre-defined global disc model.

2.1 Model and governing equations

2.1.1 Global disc model

At a distance r from a Sun-like star of radius $\mathrm{R}_\odot = 6.957 \times 10^{10}$ cm and effective temperature $T_\odot = 5777$ K, the equilibrium blackbody temperature of a disc is:

$$T_{\rm bb} = T_\odot \left(\frac{\mathrm{R}_\odot}{r}\right)^{1/2} \left(\frac{h}{r}\right)^{1/4}, \tag{1}$$

depending on the passive opening angle of the disc

$$\frac{h}{r} = \left(\frac{k_{\rm B}\, T_\odot \sqrt{\mathrm{R}_\odot r}}{\mu m_{\rm H} G M_\odot}\right)^{4/7}, \tag{2}$$

see, for example Dullemond (2000). In these equations, $k_{\rm B}$ is Boltzmann's constant, $\mu = 2.353$ is the mean molecular weight of the gas for a prescribed solar composition, $m_{\rm H}$ the hydrogen mass, and $\mathrm{M}_\odot = 1.989 \times 10^{33}$ g the mass of the Sun. We take solar parameters for simplicity, noting that representative protostars might have larger radii and lower effective temperatures.

We prescribe the mass surface density of the disc $\Sigma = 1.7 \times 10^3 (r/1\mathrm{au})^{-3/2}\,\mathrm{g\,cm^2}$ consistently with the Minimum Mass Solar Nebula (Hayashi 1981) to facilitate comparisons with previous works. Although recent surveys point toward shallower density profiles $\Sigma \sim r^{-1/2}$ (Andrews & Williams 2007; Tazzari et al. 2017), using a steeper density profile allows us to sample a broader range of disc conditions and thus cover the uncertainties in disc masses and ages (Bergin & Williams 2017).

2.1.2 Stratified shearing sheet

At a chosen radius r around the star, we move into a reference frame orbiting at the local orbital frequency Ω and expand the potential of the star to second order following the 'shearing sheet' approximation (Hill 1878; Goldreich & Lynden-Bell 1965; Latter & Papaloizou 2017). We obtain the vertical structure of the disc at this radius by integrating the equations of radiative MHD in the shearing sheet.

We describe the gas as a mixture of neutrals, ions, and electrons, with the neutrals dominating the gas mass and the free electrons being the mobile charge carriers. Denoting by ρ the neutral gas density, $\boldsymbol{u}$ its velocity, and $\boldsymbol{B} = B\boldsymbol{e_B}$ the magnetic (induction) field, their evolution in time is governed by:

$$D_t \rho = -\rho \nabla \cdot \boldsymbol{u}, \tag{3}$$

$$D_t \boldsymbol{u} = -\frac{1}{\rho}\nabla P - 2\Omega \boldsymbol{e}_z \times \boldsymbol{u} + 2q\Omega^2 x \boldsymbol{e}_x - \Omega_z^2 z \boldsymbol{e}_z - \frac{\boldsymbol{J}\times\boldsymbol{B}}{\rho}, \tag{4}$$

$$D_t \boldsymbol{B} = \boldsymbol{B}\cdot\nabla\boldsymbol{u} + \nabla\times\boldsymbol{\mathcal{E}}, \tag{5}$$

where we introduced the operator $D_t = \partial_t + \boldsymbol{v}\cdot\nabla$, the shear rate $q = -\mathrm{dlog}\,\Omega/\mathrm{dlog}\,r$ and the vertical epicyclic frequency Ω_z. In equation (5), $\boldsymbol{\mathcal{E}}$ is the electric field in a frame comoving with the neutral fluid (detailed in Section 2.1.4) and $\boldsymbol{J} = \nabla\times\boldsymbol{B}$ is the electric current neglecting relativistic effects.

For the gas pressure P we consider an ideal diatomic gas with a single adiabatic index $\gamma = 7/5$. Denoting E_R the frequency-integrated radiation energy density, the gas pressure and radiation energy are coupled via

$$D_t P = -\gamma P \nabla\cdot\boldsymbol{u} - (\gamma-1)\frac{c}{\lambda}\left(aT_\mathrm{g}^4 - E_\mathrm{R}\right) + (\gamma-1)Q, \tag{6}$$

$$\partial_t E_\mathrm{R} = -\nabla\cdot\boldsymbol{F}_\mathrm{R} + \frac{c}{\lambda}\left(aT_\mathrm{g}^4 - E_\mathrm{R}\right), \tag{7}$$

where c is the speed of light, λ is the photon mean-free path, $a \equiv 4\sigma_\mathrm{SB}/c$ with σ_SB the Stefan–Boldzmann constant, $T_\mathrm{g} = P/\rho$ is the gas temperature, Q is the heating power density of dissipative effects, and $\boldsymbol{F}_\mathrm{R}$ is the flux of radiative energy (detailed in Section 2.1.5).

We consider axisymmetric equilibria that vary on global scales radially. In the shearing sheet these radial variations are neglected and thus our local solutions depend only on the vertical coordinate – pointing along the axis of rotation and denoted by z. Although the radial coordinate (usually denoted by x) disappears in the final form of the equations, the radial shear of the flow still affects the momentum and magnetic induction equations.

Furthermore, we neglect the radial pressure gradient in the disc by considering that it orbits the star at the Keplerian frequency[1] for every z. In this case, the shear rate $q = 3/2$ and $\Omega_z = \Omega$. The shearing-sheet equations (3) and (4) then support the steady isothermal solution of a Keplerian shear flow $\partial_x u_y = -(3/2)\Omega$.

Despite these simplifications, the problem retains complexity in the details of the electromotive field $\mathcal{E}$ and radiative energy flux F_R. We describe these terms in the following paragraphs and give the final form of the radiative MHD equations in Section 2.1.6.

2.1.3 *Ionization fraction*

Solving for the detailed chemical composition of the gas in a dusty environment is expensive in computational time and subject to strong assumptions. We use the same simplifications as Lesur et al. (2014) to evolve the ionization fraction x_e in time as a balance between the local ionization versus recombination rates. In particular, we consider a metal and dust-free environment of primordial chemical composition (75 per cent hydrogen).

The ionization rate includes contributions from stellar X-rays (Igea & Glassgold 1999) using the fit of Gressel et al. (2015, first term of equation 4), cosmic rays with a penetration depth of 96 g cm^{-2} (Umebayashi & Nakano 1981), and radioactive decay at a constant ionization rate of 10^{-19} s^{-1} (Umebayashi & Nakano 2009). The X- and cosmic ray fluxes are assumed to penetrate the disc vertically from both sides. We neglect collisional ionization at the temperatures $< 10^3$ K considered.

Including dust grains and/or metals can alter the ionization fraction by several orders of magnitude depending on their abundance and distribution in the disc (e.g. Sano et al. 2000; Fromang, Terquem & Balbus 2002; Wardle 2007). A simple way to account for the dust-enhanced recombination rate is to artificially reduce the ionization fraction. We therefore include models with an ionization fraction x_e reduced by a factor 10^{-2} in Section 3.4 and 10^{-3} in Section 4.

Far-ultraviolet (FUV) stellar radiations can ionize carbon and sulfur in the uppermost layers of the disc, providing a floor value $x_e \geq 10^{-5}$ down to column densities $\lesssim 10^{-2}$ g cm^{-2} ($z/h \approx 4$, Perez-Becker & Chiang 2011). We do not include this source of ionization because it favours variability in the uppermost layers of the disc and hinders convergence to steady states (Riols et al. 2016). The ionization profiles corresponding to the reference model described above are drawn on Fig. 1.

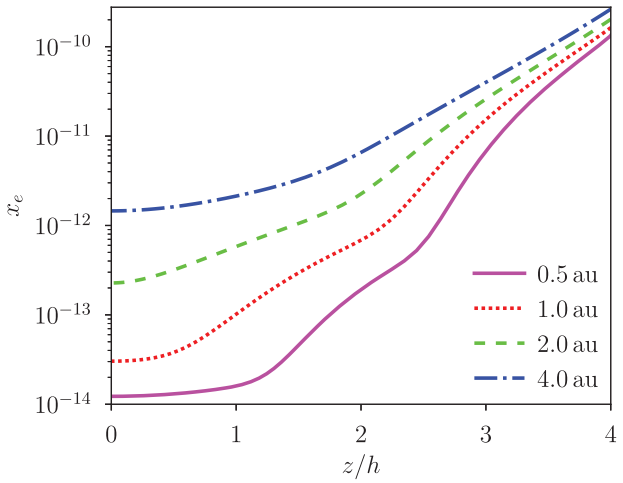

Figure 1. Vertical profiles of ionization fraction x_e for an isothermal disc of temperature T_bb given by (1) at different disc radii (see the legend).

2.1.4 *Electric conductivity*

At such low ionization fractions $x_e \lesssim 10^{-10}$, the plasma imperfectly conducts electric currents. In the frame comoving with the neutral gas, the electric field can be related to the electric current by a generalized Ohm's law:

$$\boldsymbol{\mathcal{E}} = -\underbrace{\boldsymbol{u}\times\boldsymbol{B}}_{\text{ideal}} + \underbrace{\eta_\mathrm{O}\boldsymbol{J}}_{\text{Ohm}} + \underbrace{\eta_\mathrm{H}\boldsymbol{J}\times\boldsymbol{e_B}}_{\text{Hall}} - \underbrace{\eta_\mathrm{A}(\boldsymbol{J}\times\boldsymbol{e_B})\times\boldsymbol{e_B}}_{\text{ambipolar}}, \tag{8}$$

The 'non-ideal' diffusivities $\eta_{\mathrm{O,H,A}}$ are evolved as in Lesur et al. (2014) assuming that the plasma is composed of neutrals, electrons, and ions; we do not include dust grains as charge carriers.

The relative importance of the three non-ideal MHD effects can be characterized by appropriately normalizing the diffusivities $\eta_{\mathrm{O,H,A}}$. Let $v_\mathrm{A} \equiv B/\sqrt{\rho}$ denote the Alfvén velocity. The vertical profiles of $\eta_\mathrm{O}/\Omega h^2$, $\eta_\mathrm{H}/hv_\mathrm{A}$, and $\Omega\eta_\mathrm{A}/v_\mathrm{A}^2$ are drawn on Fig. 2 at a distance of 0.5 and 4 au from the star in the passive and vertically isothermal disc described in Section 2.1.1. These dimensionless numbers are independent of the strength of the magnetic field and can be used to determine the linear stability of the disc to the MRI (see Section 3.1, and references therein).

2.1.5 *Radiative energy flux*

We solve for the frequency-integrated radiation energy density E_R in the flux-limited-diffusion (FLD) approximation. We compute the frequency-integrated opacity κ as a function of the local gas temperature T_g and neutral gas density ρ using the tables of Bell & Lin (1994). The photon mean-free path is $\lambda \equiv 1/\kappa\rho$ and the optical depth $\tau(z) \equiv -\int_\infty^z \kappa\rho\,\mathrm{d}z'$ is integrated toward the disc mid-plane.

In the FLD approximation, the radiative energy flux is

$$F_\mathrm{R} = -f_\mathrm{M} c\lambda\frac{\partial E_\mathrm{R}}{\partial z}. \tag{9}$$

[1]The deviations from Keplerian velocity scale as h/r relative to the sound speed, that is at most 3.7×10^{-2} in the model considered here, see Table 1. We also neglect the vertical shear $\partial_z u_y$ induced by the radial temperature profile (1) of the passive disc (e.g. Urpin 1984).

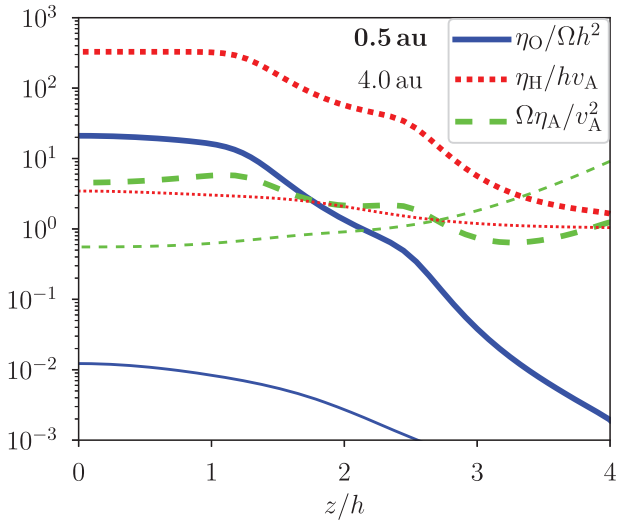

Figure 2. Vertical profiles of dimensionless numbers characterizing the strength of Ohmic (solid blue), Hall (dotted red), and ambipolar (dashed green) diffusivities for a vertically isothermal disc at 0.5 au (thick lines) and 4.0 au (thin lines) with the ionization fractions shown on Fig. 1.

where the flux limiter f_M of Minerbo (1978) allows a smooth transition from the optically thick regime $F_R \simeq -(\lambda c/3)\partial_z E_R$ to the optically thin regime $F_R \simeq -cE_R(\partial_z E_R/|\partial_z E_R|)$. The radiation pressure $E_R/3$ is typically 10^{-6} times smaller than the gas pressure in the regime considered, so we neglect momentum exchanges between the gas and radiation field.

The stellar irradiation is incorporated in the problem by imposing the radiation temperature $T_R \equiv \sqrt[4]{E_R/a}$ at low optical depth above the disc. This approach provides the correct blackbody temperature in the optically thick parts of a passive disc while ignoring the details of heat deposition in its surface layers.

2.1.6 *Governing equations*

Solving for the deviations from the background Keplerian shear $\boldsymbol{v} = \boldsymbol{u} - (3/2)\Omega x \boldsymbol{e}_y$, we look for steady states of the following system of equations:

$$\frac{\partial \rho}{\partial t} = -\frac{\partial}{\partial z}(\rho v_z), \tag{10}$$

$$\frac{\partial v_x}{\partial t} = 2\Omega v_y - v_z\frac{\partial v_x}{\partial z} + \frac{J_y B_z}{\rho}, \tag{11}$$

$$\frac{\partial v_y}{\partial t} = -\frac{1}{2}\Omega v_x - v_z\frac{\partial v_y}{\partial z} - \frac{J_x B_z}{\rho}, \tag{12}$$

$$\frac{\partial v_z}{\partial t} = -\frac{\partial}{\partial z}\left(\frac{1}{2}v_z^2 + \frac{1}{2}\Omega^2 z^2\right) - \frac{1}{\rho}\frac{\partial}{\partial z}\left[P + \frac{1}{2}\left(B_x^2 + B_y^2\right)\right] + \Omega h^2 \partial_z^2 v_z, \tag{13}$$

$$\frac{\partial B_x}{\partial t} = \frac{\partial \mathcal{E}_y}{\partial z}, \tag{14}$$

$$\frac{\partial B_y}{\partial t} = -\frac{\partial \mathcal{E}_x}{\partial z} - \frac{3}{2}\Omega B_x, \tag{15}$$

$$\frac{\partial P}{\partial t} = -v_z\frac{\partial P}{\partial z} - \gamma P\frac{\partial v_z}{\partial z} - (\gamma-1)\frac{c}{\lambda}\left(aT_g^4 - E_R\right) + (\gamma-1)\left[\eta_O\left(J_x^2 + J_y^2\right) + \eta_A\left(J_{\perp x}^2 + J_{\perp y}^2 + J_{\perp z}^2\right)\right], \tag{16}$$

Table 1. Characteristics of the chosen disc model at different radii: gas surface density Σ, passive opening angle h/r, blackbody disc temperature T_{bb}, altitude z_τ of the $\tau = 1$ surface, and vertically averaged opacity $\overline{\kappa}$.

r (au)	Σ (g cm^{-2})	h/r	T_{bb} (K)	z_τ/h	$\overline{\kappa}$ (cm^2 g^{-1})
0.5	4.81×10^3	2.04×10^{-2}	211	3.58	1.47
1.0	1.70×10^3	2.49×10^{-2}	156	3.58	4.27
2.0	6.01×10^2	3.03×10^{-2}	116	3.22	2.70
4.0	2.13×10^2	3.70×10^{-2}	86	2.73	1.49

$$\frac{\partial E_R}{\partial t} = -\frac{\partial F_R}{\partial z} + \frac{c}{\lambda}\left(aT_g^4 - E_R\right). \tag{17}$$

The last term in equation (13) acts as a viscosity to damp vertical motions, allowing the disc to relax to an equilibrium. In equation (16), ambipolar heating appears as a function of the electric current projected perpendicularly to the local magnetic field: $\boldsymbol{J}_\perp = -(\boldsymbol{J} \times \boldsymbol{e}_B) \times \boldsymbol{e}_B = \boldsymbol{J} - (\boldsymbol{J}\cdot\boldsymbol{e}_B)\boldsymbol{e}_B$.

2.1.7 *Units and conventions*

We can identify a set of natural scales in this problem. The orbital frequency Ω is taken as inverse time unit. The passive scale height h of the disc – without internal heating – is taken as distance unit. The velocity unit is therefore the passive sound speed $c_s = \Omega h$. Note that the actual density stratification scale varies and becomes larger than h when the temperature increases inside the disc. The gas temperature $T_g \equiv P/\rho$ is normalized by the surface blackbody value T_{bb}. Finally, the gas surface density Σ defines a mass unit.

The degree of magnetization of the disc is measured by the dimensionless parameter

$$\beta \equiv \frac{\Sigma\Omega^2 h}{B_z^2}. \tag{18}$$

For an isothermal hydrostatic equilibrium, β is approximately 20 per cent larger than the mid-plane ratio of thermal versus magnetic pressures $\beta_0 \equiv 2\rho c_s^2/B_z^2$.

Table 1 gathers typical values of our disc model at different radii. The choice of disc radius strongly affects the surface density of the gas and only weakly its blackbody temperature. In turn, the surface density controls the MHD diffusivities and the gas opacity.

2.2 Numerics

We obtain the steady-state vertical structure of the disc by an initial value approach. We integrate the equations (10)–(17) in time until a steady-state criterion is satisfied. This method does not require a good guess of the solution to start with, and it guarantees that the steady-state solutions are stable to disturbances of the flow variables that only depend on the vertical direction.

2.2.1 *Computational domain*

We only solve the equations on the upper half of the disc ($z \geq 0$), and assume that our solutions exhibit an equatorial symmetry about the mid-plane. This choice helps reduce computational costs while allowing control of the mid-plane conditions to machine accuracy.

The vertical domain is fixed to $z/h \in [0, 4]$ throughout this paper. As long as the effective scale height of the disc is approximately h, most of the gas mass and electric current are located inside the

computational domain. This domain also encloses the $\tau = 1$ altitude, so it captures the transition from the optically thin upper regions ($\lambda/h \gtrsim 1$) to the optically thick mid-plane ($\lambda/h \ll 1$). Convergence with domain size is discussed in Appendix C.

The domain is meshed with 64 Gauss–Lobatto points to perform Chebyshev differentiation and integration by simple matrix-vector products. This spectral decomposition provides the maximal accuracy for smooth solutions at the cost of numerical resilience when the flow variables exhibit sharp gradients.

2.2.2 *Integration scheme*

The scale separation between the radiative, MHD diffusive, and sound-crossing time makes the problem computationally inaccessible to purely explicit integration schemes. We therefore integrate the equations via a fully implicit scheme for all the flow variables. Because our interest is in steady states we can adopt first-order integration without concerns over time-accuracy. We demonstrate in Appendix B that this numerical scheme does capture the growth of MRI modes both in space and time.

We rescale the flow variables to have similar amplitudes and cast the system of equations (10)–(17) in the form $\partial_t f - S(f) = 0$. We stop the integration when a solution satisfies the simple steady-state criterion $\|(\partial_t f)/\Omega f\|_\infty < 10^{-4}$. The residual error generally keeps converging to zero when this criterion is satisfied.

2.2.3 *Initial and boundary conditions*

We start the time integration close to the 'current-free' equilibrium

$$\begin{pmatrix} \rho \\ v_x,\, v_y,\, v_z \\ B_x,\, B_y,\, B_z \\ P \\ E_\mathrm{R} \end{pmatrix} (z, t=0) = \begin{pmatrix} \rho_0 \exp(-z^2/2h^2) \\ 0,\ 0,\ 0 \\ 0,\ 0,\ \beta^{-1/2} \\ \rho_0 c_s^2 \exp(-z^2/2h^2) \\ a T_\mathrm{bb}^4 \end{pmatrix}, \tag{19}$$

consisting of the isothermal Keplerian flow with a vertical magnetic field $B_z \neq 0$ in it. The density is normalized so that $\int_0^{4h} \rho \,\mathrm{d}z = \Sigma/2$.

On top of this equilibrium, the horizontal velocity and magnetic field components are initialized with random noise ($\tilde{v}_x$, $\tilde{v}_y$, $\tilde{B}_x$, $\tilde{B}_y$) of amplitude 10^{-4}. To speed-up parametric explorations, a previously computed solution is re-used as the initial condition if only one control parameter has changed since.

We enforce an equatorial symmetry at the mid-plane via

$$(\partial_z \rho,\ \partial_z v_x,\ \partial_z v_y,\ v_z,\ B_x,\ B_y,\ \partial_z P,\ \partial_z E_\mathrm{R})(z=0, t) = 0. \tag{20}$$

These conditions will pick out equilibria that exhibit 'hourglass' magnetic configurations through the mid-plane. We consider two possible sets of boundary conditions at the top of the domain. The first set is

$$\begin{pmatrix} v_z,\ \partial_z B_x,\ \partial_z B_y, \\ E_\mathrm{R} \end{pmatrix} (z=4h, t) = \begin{pmatrix} 0,\ 0,\ 0 \\ a T_\mathrm{bb}^4 \end{pmatrix} \tag{21}$$

while we let the other flow variables relax to stationary values. Note that equation (21) does not impose the orientation nor strength of the magnetic field, which the system select itself. This set of conditions will be associated with 'internally driven' equilibria in Section 3. The second set of boundary conditions differs from equation (21) only by imposing the value $B_y^\mathrm{top} \equiv B_y(4h) \neq 0$, and will be associated with 'externally driven' states in Section 4.

2.3 Diagnostics

We measure the gas temperatures T_0 at the mid-plane and T_τ at the $\tau = 1$ altitude. We define the temperature contrast as $(T_0 - T_\tau)/T_\tau$. We define the specific entropy $s \equiv P/\rho^\gamma$ and deduce the squared Brünt–Väisälä frequency:

$$\mathcal{N}^2 \equiv \frac{\Omega^2 z}{\gamma s} \frac{\partial s}{\partial z}. \tag{22}$$

Negative values of $\mathcal{N}^2 < 0$ imply convective instability in a purely hydrodynamic disc with no viscosity or thermal diffusion (Ruden, Papaloizou & Lin 1988; Held & Latter 2018), and assuming that non-ideal MHD effects erase any stabilization from magnetic tension. We define the Brünt–Väisälä growth rate $\omega \equiv \sqrt{-\mathcal{N}^2}$ when $\mathcal{N}^2 < 0$ and zero otherwise.

The surface value of the azimuthal magnetic field B_y^top can be related to the net electric current passing through the disc via

$$B_y^\mathrm{top} = \int_0^{4h} -J_x \,\mathrm{d}z, \tag{23}$$

and to the mass accretion rate $\dot{M} = 2\int_0^{4h} \rho v_x \,\mathrm{d}z$ after multiplying equation (12) by ρ and integrating:

$$B_y^\mathrm{top} = \frac{\Omega \dot{M}}{4 B_z}. \tag{24}$$

This last equation connects the net mass accretion rate to the angular momentum extracted vertically by the magnetic stress $-B_y^\mathrm{top} B_z$.

In steady state, the condition $v_z = 0$ at the boundaries enforce $v_z = 0$ everywhere, that is no advective flux of kinetic or thermal energy through the domain. The pressure equation (16) then becomes a competition between Ohmic and ambipolar heating versus radiative cooling. To measure their influence on the gas temperature, we introduce the respective heating/cooling rates per unit mass:

$$\partial_t P = \rho(q_\mathrm{O} + q_\mathrm{A} + q_\mathrm{R}) = 0, \tag{25}$$

where q_O denotes Ohmic heating, q_A ambipolar heating, and q_R radiative cooling. We also define the total energy density

$$E \equiv \frac{1}{2}\rho \boldsymbol{v}\cdot\boldsymbol{v} + \frac{1}{2}\boldsymbol{B}\cdot\boldsymbol{B} + \frac{1}{\gamma - 1}P + E_\mathrm{R}. \tag{26}$$

If $\boldsymbol{L} \equiv \boldsymbol{J} \times \boldsymbol{B}$ is the Lorentz force and $v_z = 0$ because of boundary conditions, then the evolution of the total energy density (26) obeys

$$\begin{aligned} \partial_t E = &+\frac{3}{2}\Omega(\rho v_x v_y - B_x B_y) && \text{sources} \\ &- \partial_z[(v_x B_x + v_y B_y) B_z] && \text{ideal} \\ &- \partial_z[(J_x B_y - J_y B_x)\eta_\mathrm{O}] && \text{Ohmic} \\ &- \partial_z[(L_x B_y - L_y B_x)\eta_\mathrm{H}] && \text{Hall} \\ &- \partial_z[(J_{\perp x} B_y - J_{\perp y} B_x)\eta_\mathrm{A}] && \text{ambipolar} \\ &- \partial_z F_\mathrm{R} && \text{radiation.} \end{aligned} \tag{27}$$

It comprises a single source term, arising from the extraction of orbital energy by the combined action of Reynolds and Maxwell stresses. The subsequent terms represent the ideal MHD Poynting flux, three energy fluxes due to non-ideal MHD effects and the radiative energy flux. As emphasized throughout this paper, the four fluxes of magnetic energy are thermodynamically crucial because they can redistribute orbital energy away from the height at which it was originally extracted, and before this energy is be thermalized.

The heat generated by electron-neutral (Ohmic) and ion-neutral (ambipolar) collisions is integrated vertically to define the electric

heat fluxes per unit surface of the disc:

$$Q_{\rm O} \equiv \int_0^{4h} \eta_{\rm O} \left(J_x^2 + J_y^2\right) \mathrm{d}z = \int_0^{4h} \frac{\rho q_{\rm O}}{\gamma - 1} \mathrm{d}z, \tag{28}$$

$$Q_{\rm A} \equiv \int_0^{4h} \eta_{\rm A} \left(J_{\perp x}^2 + J_{\perp y}^2 + J_{\perp z}^2\right) \mathrm{d}z = \int_0^{4h} \frac{\rho q_{\rm A}}{\gamma - 1} \mathrm{d}z. \tag{29}$$

Integrating equation (27) vertically and substituting equations (16) and (17) in steady state, we can connect the heat fluxes with the radial flux of angular momentum through the disc:

$$\frac{3}{2}\Omega \int_0^{4h} (\rho v_x v_y - B_x B_y)\, \mathrm{d}z = Q_{\rm O} + Q_{\rm A} + F_z^{\rm top}, \tag{30}$$

where $F_z^{\rm top}$ is the magnetic energy flux (ideal, Ohmic, Hall, and ambipolar) through the upper boundary $z = 4h$.

Normalizing the heat fluxes into a dissipation coefficient

$$\alpha \equiv \frac{8}{9} \frac{Q_{\rm O} + Q_{\rm A}}{\Sigma h^2 \Omega^3}, \tag{31}$$

we can relate stress and dissipation in the standard framework of α discs (Balbus & Papaloizou 1999). When no magnetic energy flows through the upper boundary, $F_z^{\rm top} = 0$ and we have

$$\int_0^{4h} (\rho v_x v_y - B_x B_y)\, \mathrm{d}z = \frac{3}{4} \alpha \Sigma h^2 \Omega^2. \tag{32}$$

On the other hand, it the energy extracted by the internal xy stress is negligible compared to the energy flux $F_z^{\rm top}$ at the surface of the disc, we obtain the balance:

$$F_z^{\rm top} = -\frac{9}{8} \alpha \Sigma h^2 \Omega^3. \tag{33}$$

3 INTERNALLY DRIVEN STATES

3.1 Instability of the current-free equilibrium

Integrating the system (10)–(17) in time subject to the boundary conditions (21), the flow can follow two different routes depending on the stability of the current-free equilibrium (19). Although a linear stability analysis is outside the scope of this paper, we can identify the cause of the instability in our simulations.

In ideal MHD, weakly magnetized Keplerian flows are subject to the MRI (Balbus & Hawley 1991). In a 1D shearing box (vertical structures only), the MRI can be stabilized by both Ohmic (Jin 1996) and ambipolar diffusion (Desch 2004; Kunz & Balbus 2004). The Hall effect can be either stabilizing or destabilizing depending on the strength and orientation of the net magnetic field (Wardle 1999; Balbus & Terquem 2001). For the Hall-dominated regime probed in this paper, the HSI appears while the MRI is resistively damped (Kunz 2008; Wardle & Salmeron 2012).

If the current-free equilibrium is linearly stable, then the MHD diffusivities dissipate electric currents and let the flow relax to the same equilibrium. Otherwise, the initial perturbations grow exponentially in time and amplify the electric current and magnetic stress through the disc. Since the 1D shearing box forbids the development of 'parasitic' secondary instabilities (Goodman & Xu 1994; Latter, Fromang & Gressel 2010; Kunz & Lesur 2013), the exponential growth saturates in the non-linear regimes of Hall and ambipolar diffusion. This saturation happens before magnetic pressure significantly alters the disc structure.

The linear phase of the instability is illustrated in Appendix B. The dissipative effects allow the system to reach a steady state which only depends on the choice of (r, β) and not on the initial noise. We qualify these states as 'internally driven' because they are powered by the orbital shear and satisfy equation (32). For the magnetizations $\beta \in [10^3, 10^8]$ considered, the $B_z < 0$ cases are always linearly stable; we therefore focus on the $B_z > 0$ cases in this section.

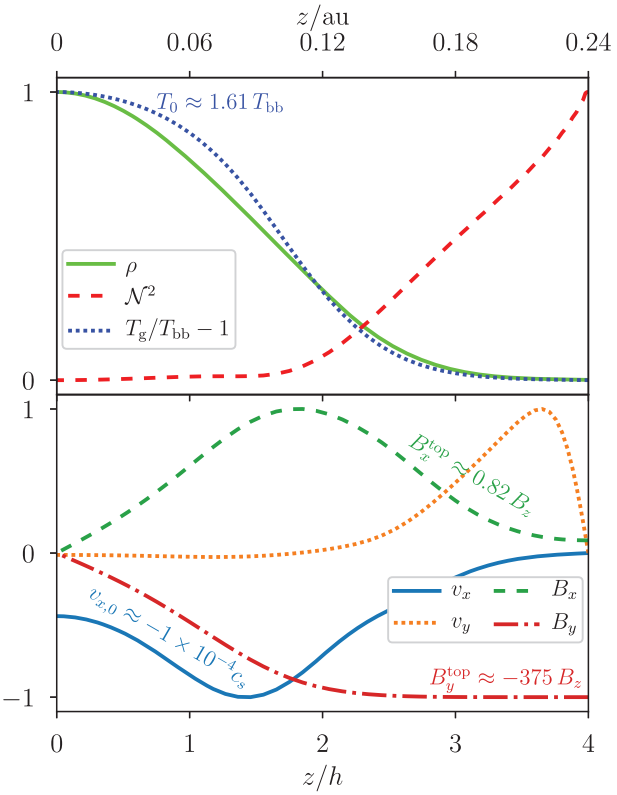

Figure 3. Vertical profiles of the flow variables in an equilibrium with $\beta = 10^7$ at $r = 2$ au, normalized by their extremal value for visibility. Upper panel: density (solid green), squared Brünt–Väisälä frequency (dashed red), and gas temperature relative to $T_{\rm bb}$ (dotted blue). Lower panel: radial velocity (solid blue), azimuthal velocity (dotted orange), radial magnetic field (dashed green), and azimuthal magnetic field (dotted–dashed red).

3.2 Reference solution

We start by exhibiting the properties of a reference solution computed at $r = 2$ au with $\beta = 10^7$. Since the relative importance of non-ideal MHD effects varies with radius, we provide a second example solution computed at $r = 1$ au in Appendix A.

3.2.1 *Vertical structure*

Fig. 3 shows the vertical profiles of the flow variables in a steady state computed at $r = 2$ au with $\beta = 10^7$; the curves have been rescaled to fit in $[-1, 1]$ for visibility.

The thermodynamic variables are represented on the upper panel. The density distribution is close to Gaussian; it is always decreasing with height ($\partial_z \rho \leq 0$), as for every equilibria presented in this paper. The gas temperature is maximal in the mid-plane where it reaches $T_{\rm g} \approx 1.61 T_{\rm bb}$. It is equal to the radiation temperature to 10^{-6} accuracy on the entire interval (not shown). The squared Brünt–Väisälä frequency $\mathcal{N}^2 > 0$ everywhere, so this equilibrium is convectively stable. However, $\mathcal{N}^2 \approx 0$ for $z/h \lesssim 2$ implies that the deep disc is close to marginal stability. Other solutions do exhibit entropy profiles decreasing with height, see Section 3.3.3.

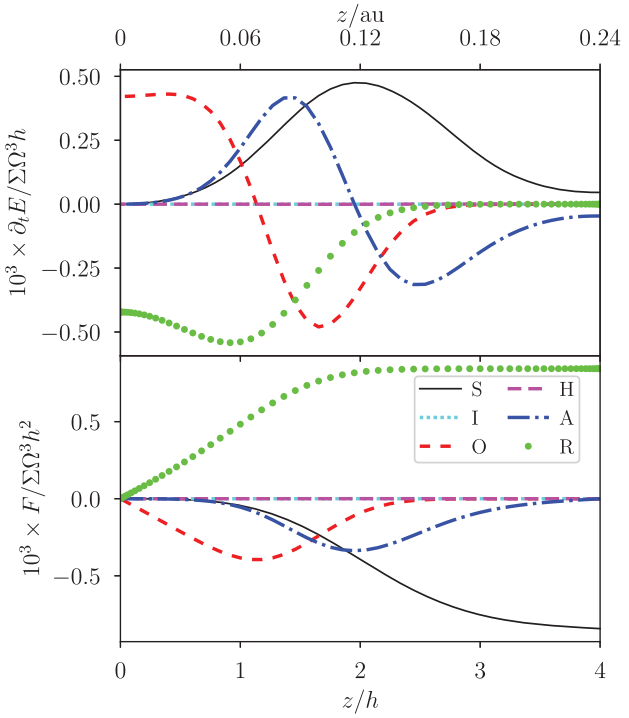

Figure 4. Energy budget in the same equilibrium as on Fig. 3. Upper panel: total energy equation (27). Lower panel: associated energy fluxes, equivalent to the vertical integral of equation (27) from the mid-plane. The different curves correspond to the source term ('S', solid black), the ideal induction ('I', dotted cyan), Ohmic resistivity ('O', dashed red), the Hall drift ('H', dashed magenta), ambipolar diffusion ('A', dotted–dashed blue), and radiation ('R', green dots).

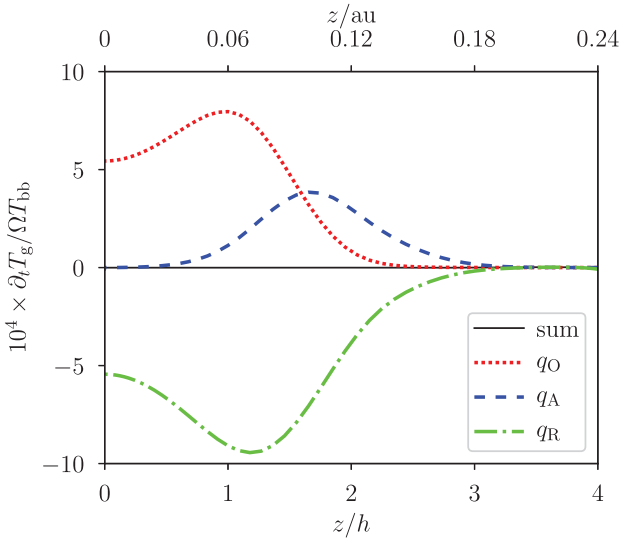

Figure 5. Heating/cooling rates per unit mass as defined in equation (25) for the same equilibrium as on Fig. 3. Ohmic (q_O, dotted red) and ambipolar heating (q_A, dashed blue) are balanced by radiative cooling (q_R, dotted–dashed green).

The MHD variables are represented on the lower panel, where the velocities correspond to deviations from the Keplerian background. The azimuthal velocity v_y is negative near the mid-plane and positive in the surface layers, indicating that angular momentum has been exchanged between the two layers. The radial velocity v_x has a constant sign, so there is a net mass accretion rate $\dot{M} = \int \rho v_x \, \mathrm{d}z \neq 0$ in the entire domain.[2] The mid-plane radial velocity is only $-1 \times 10^{-4} c_s$ so the accretion flow is very subsonic. The horizontal magnetic field (B_x, B_y) grows from zero in the mid-plane to its maximal amplitude over a scale $\sim h$. The product $-B_x B_y \geq 0$ generates a radial flux of angular momentum (Maxwell stress) through the disc. The azimuthal component $B_y^{\mathrm{top}} \approx -375 B_z$ at the upper boundary, so the magnetic field is tightly coiled and the magnetic pressure $B^2/2 \gtrsim \rho c_s^2$ above $2h$.

The relation (24) is satisfied by construction: the $-B_y^{\mathrm{top}} B_z$ stress removes angular momentum vertically and causes an accretion rate $\dot{M} \neq 0$ even in the absence of an outflow ($v_z = 0$). Unlike in global disc models, the radial flux of angular momentum – measured by $\alpha \approx 7 \times 10^{-4}$ in equation (32) for this equilibrium – cannot cause a net mass accretion rate in the shearing box.

3.2.2 *Energy budget*

To explain the buildup of heat in the mid-plane, we decompose the evolution of the total energy density in the reference simulation and plot the result in Fig. 4. The individual terms of equation (27) are represented on the upper panel. The associated fluxes are drawn on the lower panel, where the source term ('S') is integrated vertically from the mid-plane and multiplied with a minus sign to allow comparison with the other fluxes.

On the upper panel, the source term (solid black) represents the extraction of energy from the Keplerian shear into velocity and magnetic fields by the xy Reynolds and Maxwell stresses. It is maximal near $z \approx 2h$ and positive at every altitudes, increasing the total energy relative to the current-free equilibrium.

The Ohmic (dashed red) and ambipolar (dotted–dashed blue) terms both have two distinct effects on the energy content of the plasma. On one side, they locally dissipate magnetic energy into thermal energy, with no effect on the total energy density. On the other side, they diffusively spread magnetic energy away from its maximum, causing the downward energy fluxes drawn on the lower panel of Fig. 4. These fluxes vanish at the boundaries of the computational domain, so they induce no net energy gain nor loss in the equilibrium. Ambipolar diffusion dominates in the upper layers $z/h \gtrsim 2$. Ohmic diffusion is predominant at low altitudes $z/h \lesssim 1$ and it is the only term bringing energy down to the mid-plane. The Hall term (dashed magenta) can only transport energy via waves. The associated energy flux is negligible in this equilibrium.

On the upper panel, the radiative term (green dots) is negative everywhere so it removes energy from the equilibrium. This is achieved by an upward radiative flux $F_R \geq 0$ on the lower panel, transporting radiative energy from the mid-plane out of the disc. The radiative flux increases with height and becomes roughly constant above $z/h \gtrsim 2$, so the conversion from thermal to radiative energy happens mostly below this height. It is the only term balancing the net energy input caused by the source term and allowing the system to reach a thermodynamic equilibrium.

Examining the total energy budget does not reveal where the conversion from kinetic and magnetic to internal energy happens. To clarify which effect is responsible for heating the gas, we decompose the internal energy (pressure) equation into specific heating/cooling rates as in equation (25) on Fig. 5. The Ohmic and ambipolar resistivities both dissipate magnetic energy (electric currents) into

[2]The system (10)–(17) of the shearing-sheet equations is independent of x, so $\int \rho v_x \, \mathrm{d}z \neq 0$ can be interpreted as mass accretion regardless of its sign.

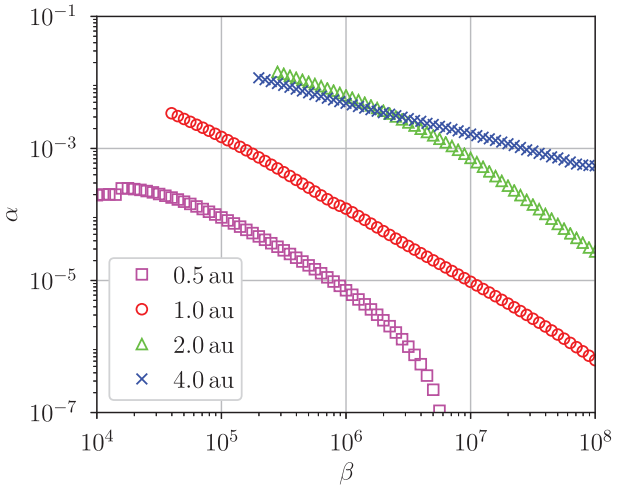

Figure 6. Dissipation coefficient α as a function of the plasma β at different radii from the star (see the legend). We stopped the exploration when the temperature contrast reached unity.

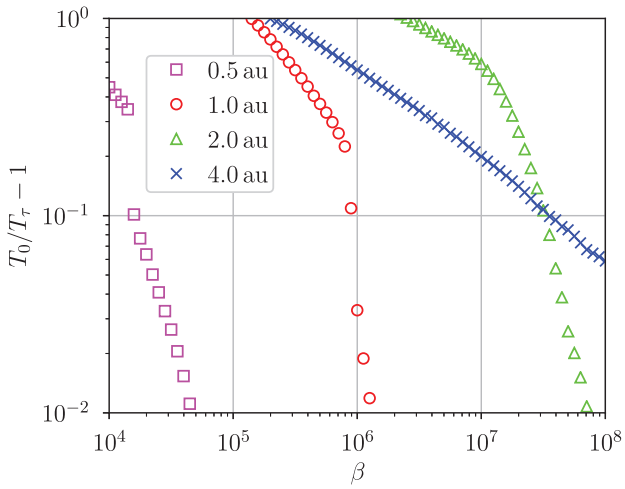

Figure 7. Temperature contrast between the mid-plane and the $\tau = 1$ altitude as a function of the plasma β at different radii from the star (see the legend).

heat. Electric heating is localized near the mid-plane and is primarily caused by Ohmic resistivity for this specific equilibrium. The radiative cooling rate q_R is the same as on the upper panel of Fig. 4 after dividing by ρ, as expected from equations (16) and (17) in steady state.

A key feature of these equilibria is that the energy extracted from the shear is redistributed vertically before being thermalized. Heating can thus occur in the mid-plane although the stress extracts orbital energy away from the mid-plane. This feature is more prominent on the alternative example solution provided in Appendix A.

3.3 Dependence on disc magnetization

We proceed to explore how our main diagnostics depend on the plasma $\beta \in [10^4, 10^8]$ at four different radii r (au) $\in \{0.5, 1, 2, 4\}$ from the star. We consistently find a one to one mapping between (r, β) and the steady-state profiles. Hence, at a given radius there seems to exist a single solution branch parametrized by β and stable to z-dependent perturbations. The remaining parameters are kept the same as in the reference equilibrium described above.

As a precaution, we stopped the exploration when the temperature contrast $T_0/T_\tau - 1$ reached unity. For larger temperature contrasts the disc becomes geometrically thicker, so our numerical domain may become insufficiently large to describe the solutions adequately. The effective scale height of the disc, measured as the standard deviation of a Gaussian profile fitting the density distribution below $3h$, is always less than $1.5h$.

3.3.1 Angular momentum transport and associated heating

We start by quantifying the radial flux of angular momentum and the associated resistive heating as expressed by equation (32). For each equilibrium, we measure the coefficient α as defined by equation (31) and place it on Fig. 6. Since we exclude solutions with a temperature contrast larger than unity, there are solutions at larger magnetizations (smaller β) than we show here: the breaks in our solutions branches are just where we end our parameter scan.

The dissipation coefficient α is a decreasing functions of β at the four radii considered. At 1 au we find that α scales roughly as $\beta^{-1/2}$, that is increases as B_z, and the scaling becomes shallower at larger radii. The values of α range from 10^{-7} to 10^{-2} over this parameter space. For a given β, the coefficient α increases by more than one order of magnitude from 0.5 to 1 au and by another order of magnitude from 1 to 2 au. We stopped the exploration when the temperature contrast in the disc reached unity, but more solutions presumably exist with $\alpha \gtrsim 10^{-2}$ for lower β. These levels of laminar magnetic stress are in agreement with the 3D stratified shearing box simulations of Lesur et al. (2014) which included the Hall effect. Ohmic heating dominates over ambipolar heating by less than a factor 10 at 0.5 and 1 au, they become comparable at 2 au and ambipolar heating dominates at 4 au (not shown).

3.3.2 Temperature contrast

Following on from the heating efficiency of these solutions, we evaluate the temperature contrast achieved between the mid-plane and the $\tau = 1$ altitude. Fig. 7 represents this temperature contrast measured for each pair of parameters (r, β).

The temperature contrast is a decreasing function of β at any given radius, so the more magnetized the disc the hotter the mid-plane compared to the surface. The temperature contrast reaches unity for $\beta \in [10^5, 3 \times 10^6]$ at $r \geq 1$ au. When going from small to larger radii, the temperature contrast becomes flatter as a function of β. At $r = 1$ au, the temperature contrast decreases from 1 to 10^{-2} over a single decade of $\beta \in [1 \times 10^5, 1 \times 10^6]$. At $r = 2$ au, the temperature contrast is larger than 10^{-2} over $\beta \in [3 \times 10^6, 7 \times 10^7]$. At $r = 4$ au, the temperature contrast is already larger than 10^{-2} at the largest $\beta = 10^8$ considered. Order unity differences between the mid-plane and surface temperatures are therefore achievable at all radii for sufficient disc magnetization.

3.3.3 Convective stability

For each equilibrium represented on Fig. 7, we compute the entropy profile via equation (22) and deduce the profile of the squared Brünt–Väisälä frequency $\mathcal{N}^2$. If $\mathcal{N}^2 < 0$ over a range of altitudes, then this range could be convectively unstable if we permitted perturbations

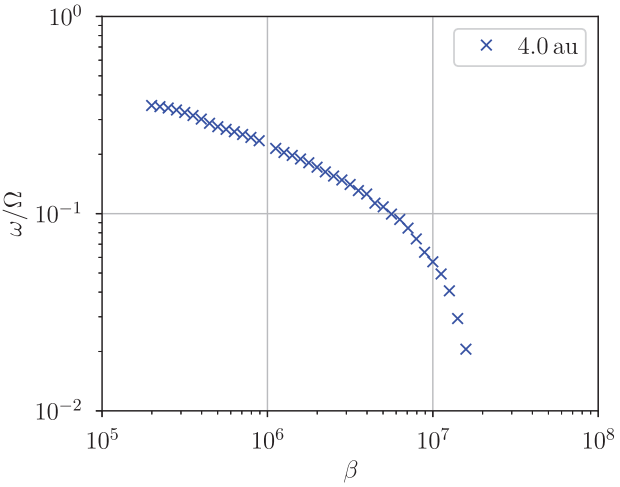

Figure 8. Maximal Brünt–Väisälä growth rate ω/Ω as a function of the plasma β, computed from the entropy profile of equilibria at different radii from the star (see the legend). We stopped the exploration when the temperature contrast reached unity.

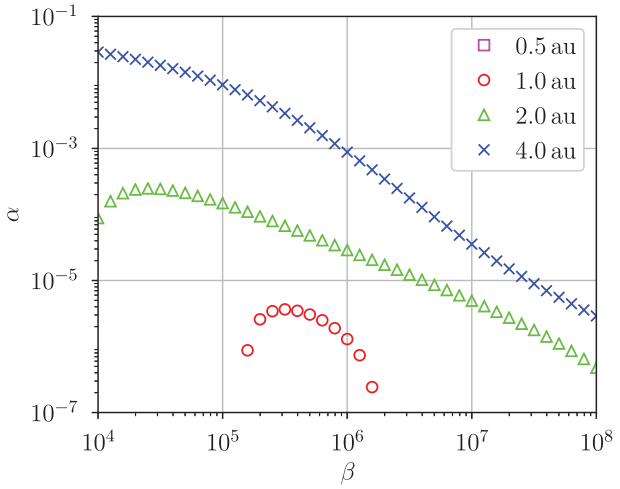

Figure 9. Same as Fig. 6 with an ionization fraction x_e reduced by a constant factor 10^{-2} at every height z/h.

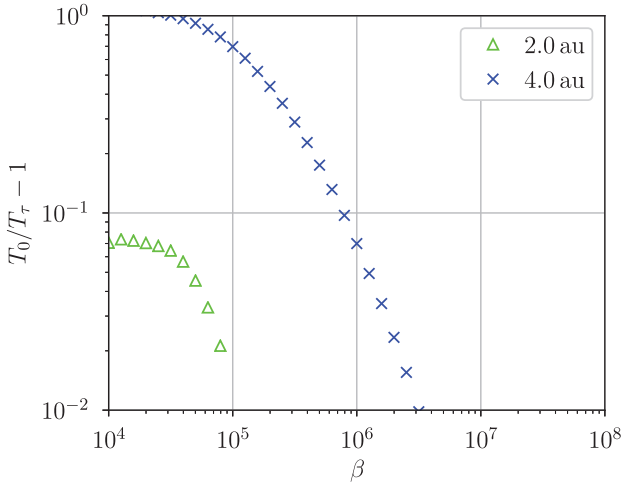

Figure 10. Same as Fig. 7 with an ionization fraction x_e reduced by a constant factor 10^{-2}; the temperature contrast remains below 10^{-2} at $r =$ 0.5 and 1 au.

with a radial dependence. The characteristic time-scale for the growth of convective modes would then be $\omega \equiv \sqrt{-\mathcal{N}^2}$. Because a full linear stability analysis is outside the scope of this paper, we focus on this necessary condition for convection.

We show the maximal value of ω/Ω measured in each equilibria over this parameter space on Fig. 8. In this disc model, only the equilibria at $r = 4$ au have a reversed entropy gradient leading to $\omega > 0$ over a range of altitudes. At $r = 4$ au, the temperature contrast reaches unity for $\beta \approx 3 \times 10^5$; more solutions with $\omega > 0$ presumably exist at lower β, which we excluded by precaution.

The Brünt–Väisälä growth rates range from a few 10^{-2} to over $3 \times 10^{-1}\Omega$ for the equilibria represented on Fig. 8. The range of altitudes over which $\omega > 0$ spans roughly $z/h \in]0, 1]$ and it expands to higher altitudes from the mid-plane as β decreases. Given the absence of viscosity and the slow radiative time-scale following from the assumed opacity, these equilibria could support unstable convective motions.

None of the solutions computed at $r \leq 2$ au have a reversed entropy gradient despite reaching order-unity temperature contrasts. Upon inspection of these solutions, the temperature profiles are flatter near the mid-plane, see for example Fig. A1 in Appendix A. When the gas temperature starts decreasing with z, the density is decreasing faster so that the specific entropy $s = T_g/\rho^{\gamma-1}$ remains monotonically increasing. To understand what controls the temperature gradient, we rewrite the radiative term in equation (25) assuming a steady-state radiation field in equation (17):

$$\rho q_R = -(\gamma - 1)\nabla \cdot F_R. \tag{34}$$

In the optically thick regions $F_R \simeq -(\lambda c/3)\nabla E_R$ with $E_R \simeq a T_g^4$ to first order. The steady-state gas temperature then satisfies

$$\nabla \cdot \left(\lambda \nabla T_g^4\right) + \frac{3}{(\gamma - 1)ac}\rho(q_O + q_A) \simeq 0, \tag{35}$$

so the mid-plane behaves as a thermal conductor with Ohmic and ambipolar heating acting as source terms. Flat temperature profiles $\partial_z T_g \ll T_{bb}/\lambda$ therefore occur when electric heating is localized away from the mid-plane. At $r = 0.5$ and 1 au, electric heating is indeed less efficient below $z \lesssim 2h$ (see Fig. A2).

3.4 Dependence on ionization fraction

To account for the possible influence of dust grains on molecular recombination and charge capture, we reduce the ionization fraction x_e by a constant factor 10^{-2} at every height. This is equivalent to increasing the MHD diffusivities $\eta \propto 1/x_e$. We show on Fig. 9 how the dissipation coefficient α varies with r and β in this more resistive case compared to Section 3.3.1.

At $r = 0.5$ au, the disc is linearly stable over the entire range of β considered: the disc converges to the current-free equilibrium (19) and therefore supports no electric heating. At $r = 1$ au, the disc is linearly unstable only for $\beta \gtrsim 10^5$. The resulting α are maximal near $\beta \approx 3 \times 10^5$ and remain weaker than $\alpha \lesssim 10^{-5}$. At $r = 2$ au, the dissipation coefficient reaches $\alpha \approx 2 \times 10^{-4}$ for $\beta = 2 \times 10^4$. At $r = 4$ au, the disc is linearly unstable for the whole range of β considered and α reaches roughly 3×10^{-2} for $\beta = 10^4$. In comparison with Fig. 6, the dissipation coefficients are 10^{-1} to 10^{-3} times lower for a given β.

Fig. 10 shows the temperature contrast $T_0/T_\tau - 1$ measured in the same series of equilibria as on Fig. 9. At $r = 0.5$ and 1 au,

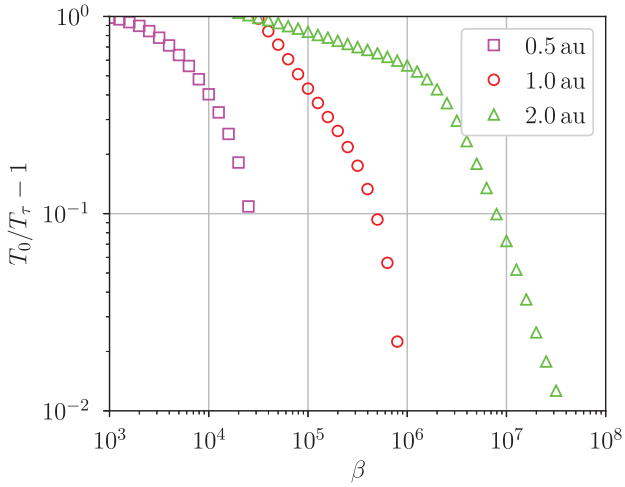

Figure 11. Same as Fig. 7 with a reduced opacity $\kappa/10$.

the temperature contrast remains below 10^{-2} for this range of disc magnetizations. At $r = 2$ and 4 au, the temperature contrast reaches its maximal value 7×10^{-2} and 1, respectively for $\beta \approx 2 \times 10^4$. The ionization fraction thus controls to a large degree the efficiency of electric heating and angular momentum transport inside the disc.

3.5 Dependence on gas opacity

For the range of temperatures considered, the frequency-integrated opacity is dominated by dust grains (Bell & Lin 1994; Ferguson et al. 2005). In the absence of vertical mixing, the sedimentation of dust grains toward the disc mid-plane and their coagulation would lower the average opacity. To account for the possible sedimentation and coagulation of dust grains, we reduce the opacity by a constant factor 10^{-1} with respect to the values of Bell & Lin (1994).

At 1 au, the altitude of the $\tau = 1$ surface in the current-free equilibrium (19) becomes $z_\tau/h \approx 2.99$, so most of the gas in the computational domain is still confined to high optical depths. The $\tau = 1$ altitude decreases to $z_\tau \approx 2.50h$ at $r = 2$ au and to $z_\tau \approx 1.86h$ at $r = 4$ au. In this last case, most of the computational domain is transparent to radiation so the vertical FLD approximation becomes inappropriate. We therefore exclude the $r = 4$ au case in this section.

Fig. 11 shows the temperature contrast obtained as a function of r and β when the opacity is reduced by a factor 10^{-1} relative to our reference case. This figure is qualitatively similar to Fig. 7, but the temperature contrast at a given β is now reduced by a factor $\approx$1/10. At $r = 2$ au, when β decreases from 10^6 to 2×10^4 the temperature contrast increases slowly from 50 per cent to unity, although the heating rate α increases from 10^{-2} to 10^{-1} (not shown). This suggests that an increasing fraction of the heating power is injected in the optically thin layers and immediately radiated away. A stronger magnetization is thus required to reach the same temperature contrast in low-opacity discs.

3.6 Mid-plane symmetry in two-sided discs

In the shearing box simulations of Lesur et al. (2014), Bai (2015), and Mori et al. (2019), the flow spontaneously adopts an 'odd' symmetry about the mid-plane. Instead of the equatorial symmetry (20) which we imposed, the odd symmetry is such that

$$(v_x, v_y, B_x, B_y)(-z) = (-v_x, -v_y, +B_x, +B_y)(z). \tag{36}$$

This symmetry allows no electric current in the mid-plane, so electric heating is necessarily localized in the surface layers $|z/h| \gtrsim 2$ (Mori et al. 2019). Since the Maxwell stress $-B_y B_z$ has a constant sign, angular momentum is injected from one boundary and extracted from the other, causing no net accretion through the disc. This odd symmetry is not only an artefact of the shearing box as it was also obtained in global disc simulations (Gressel et al. 2015; Béthune et al. 2017; Suriano et al. 2018; Rodenkirch et al. 2020).

We tested the stability of the reference solution of Section 3.2 in the two-sided domain $z/h \in [-4, +4]$. We used the symmetrized one-sided solution as initial condition, perturbed it and repeated the time integration until reaching a steady state. The flow converged to the solution with an equatorial symmetry $(B_x, B_y)(-z) = (-B_x, -B_y)(z)$ matching our standard mid-plane conditions (20). The mid-plane symmetry considered in this paper is therefore 1D stable for at least a range of radii and magnetizations.

4 EXTERNALLY DRIVEN STATES

4.1 Rationale

In Section 3.4, we reduced the ionization fraction x_e by a factor 10^{-2} and the current-free equilibrium (19) became linearly stable at $r = 0.5$ au regardless of β. When decreasing the ionization fraction by a factor 10^{-3}, the current-free equilibrium is in fact stable for all β and radii up to $r = 4$ au in our disc model. Although the instability is quenched in this regime, electric currents may still flow through the disc if an external magnetic torque $-B_y^{\rm top} B_z$ acts on the disc surface. In this case, the energy dissipated inside the disc is not extracted from the orbital shear but instead provided at the surface by an energy flux $F_z^{\rm top}$ as in equation (33).

A variety of situations can lead to such external torques if the disc is threaded by a large-scale poloidal field. These include magnetized winds (Pudritz & Norman 1983; Pelletier & Pudritz 1992) regardless of their launching mechanism – photoevaporative or magnetocentrifugal. Since the key to mass accretion and energy dissipation is the magnetic stress $-B_y^{\rm top} B_z$, as a first approximation we can neglect the outflow velocity v_z in the energetic balance (see e.g. Lovelace et al. 2002; Lovelace, Rothstein & Bisnovatyi-Kogan 2009). Alternatively, the magnetic field threading the disc might be anchored in a well-ionized medium with a different rotation rate (e.g. the star, the infalling cloud, or a different radius of the disc).

In this section, we repeat the previous calculations with two major changes. First, we decrease the ionization fraction by a factor 10^{-3} with respect to Section 2.1.3 so that the current-free equilibrium (19) is linearly stable at every radius and magnetizations considered. Second, we impose the value of $B_y^{\rm top} \equiv B_y(4h)$ at the surface of the disc, which sets the flux of angular momentum leaving the disc $-B_y^{\rm top} B_z$ and the resulting mass accretion rate via equation (24). By fixing $B_y^{\rm top}$, we set the magnetic energy flux $F_z^{\rm top}$ entering the disc in equation (33). To keep the number of free parameters to a minimum, we impose $\beta = 10^5$ and only vary the radius r and surface azimuthal field $B_y^{\rm top}$.

4.2 Reference solution

4.2.1 Vertical structure

Fig. 12 shows the vertical profiles of the flow variables in an externally driven equilibrium at $r = 1$ au with $\beta = 10^5$ and a surface

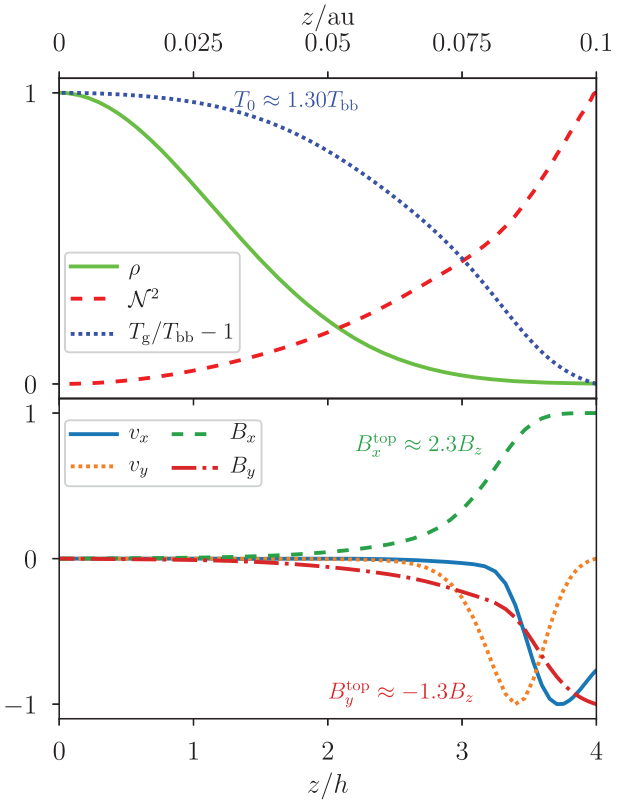

Figure 12. Vertical profiles of the flow variables in an externally driven equilibrium at $r = 1$ au with a surface azimuthal field $B_y^{\rm top} = -2 \times 10^{-2}$ G. The curves are normalized by their extremal value for visibility. Upper panel: density (solid green), squared Brünt–Väisälä frequency (dashed red), and gas temperature relative to $T_{\rm bb}$ (dotted blue). Lower panel: radial velocity (solid blue), azimuthal velocity (dotted orange), radial magnetic field (dashed green), and azimuthal magnetic field (dotted–dashed red).

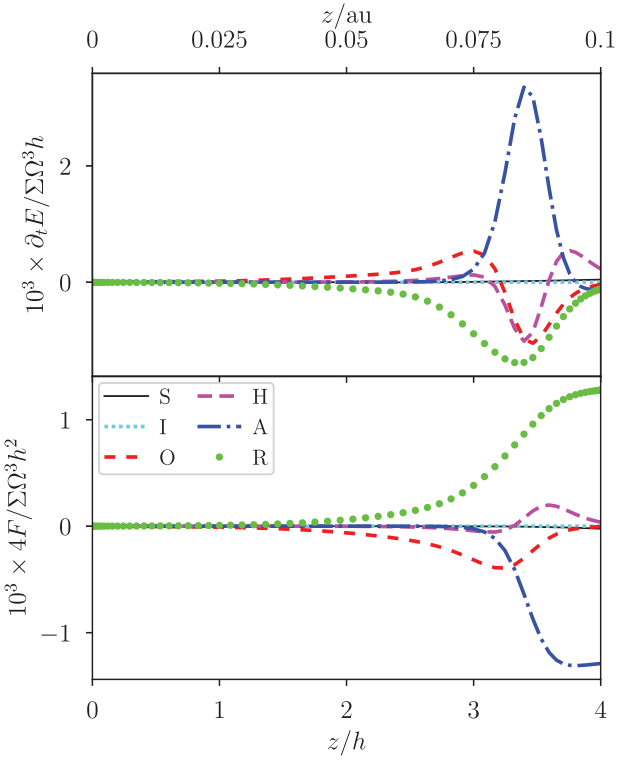

Figure 13. Same as Fig. 4 in the externally driven equilibrium of Fig. 3. The source term 'S' (solid black) is nearly zero everywhere, so energy is mainly supplied at the upper boundary.

azimuthal field $B_y^{\rm top} = -2 \times 10^{-2}$ G $\approx -1.26 B_z$. The curves have been rescaled to fit in $[-1, 1]$ for visibility.

As in the internally driven case of Fig. 3, the upper panel shows that the gas density is nearly Gaussian and the squared Brünt–Väisälä frequency $\mathcal{N}^2 > 0$ at every altitude. The gas and radiation temperatures are equal to better than 10^{-6} accuracy everywhere (not shown) and maximal in the mid-plane with $T_0 \approx 1.30 T_{\rm bb}$.

The lower panel shows that the velocity and magnetic perturbations are localized above $z/h \gtrsim 2$. The radial velocity $v_x < 0$ in an accretion layer around $z/h \approx 3.5$. Similarly the azimuthal velocity $v_y < 0$ in a narrow layer centred on $z/h \approx 3.4$. $B_y \approx 0$ in the mid-plane and its growth toward $B_y^{\rm top}$ happens rapidly above $z \gtrsim 3h$. The radial component B_x must only satisfy $\partial_z B_x = 0$ at the top boundary, so its amplitude $B_x^{\rm top} \approx 2.3 B_z$ is not fixed a priori. In this case, $B^2/2 \lesssim P$ at the surface of the disc, that is the magnetic field is nearing equipartition as expected for general accretion-ejection structures (Ferreira & Pelletier 1993). From the surface toward the mid-plane, B_x decays over a characteristic length-scale $\sim h$. Despite the electric currents being localized near the disc surface, we still find a significant build up of heat in the mid-plane.

4.2.2 *Energy budget*

On Fig. 13, we disentangle the energy exchanges in the previous externally driven equilibrium. A key difference with the internally driven state shown on Fig. 4 is that the internal stress/source term (solid black) is now negligible compared to every other contributions by two orders of magnitude. Although the product $-B_x B_y$ is non-zero on Fig. 12, the resulting stress extracts a negligible amount of energy from the Keplerian shear. In contrast to the internally driven solution (4), the energy input in this equilibrium is mainly supplied at the upper boundary and satisfies the balance (33).

As previously, the Ohmic and ambipolar fluxes transport energy downward from the disc surface. At the upper boundary, it is ambipolar diffusion that brings the energy of the imposed $B_y^{\rm top}$ (and resulting $B_x^{\rm top}$) from the surface $z = 4h$ into the disc. The Ohmic term becomes dominant near $z/h \approx 3$ and extends down to the mid-plane. The radiative flux is oriented upward in the entire domain, evacuating heat through the upper boundary and allowing the system to reach a thermodynamic equilibrium.

The vertically integrated Ohmic and ambipolar heat fluxes amount to a dissipation coefficient $\alpha \approx 7 \times 10^{-5}$ in this equilibrium. As shown above and in equation (33), this α is not related to the vertically integrated stress but to the dissipation of the energy supplied at the disc surface. We can use equation (35) to interpret the build up of heat in the mid-plane despite electric heating being localized near $z/h \approx 3$. Since the photon mean-free path increases with height ($\partial_z \lambda > 0$), radiative diffusion favours temperature maxima in the mid-plane ($\partial_z^2 T_{\rm g} < 0$) as long as it is optically thick.[3]

[3]During the evolution toward a steady state, the temperature initially rises where heat is deposited ($z/h \approx 3$), but this is only a transient stage.

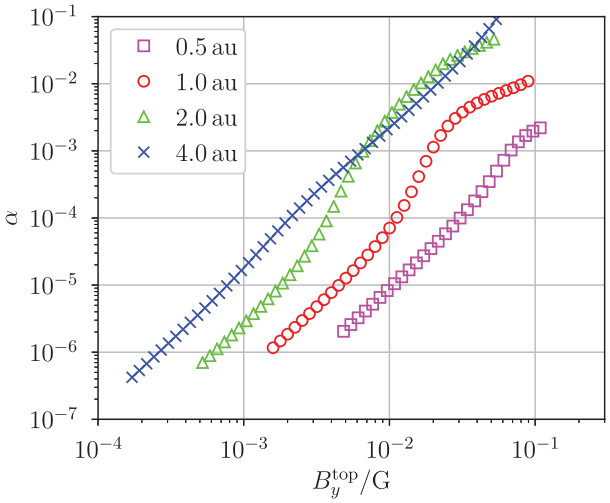

Figure 14. Dissipation coefficient α as a function of the surface azimuthal field $B_y^{\rm top}$ at different radii from the star (see the legend) in externally driven equilibria with $\beta = 10^5$. Each curve starts at $B_y^{\rm top}/B_z = 10^{-1}$.

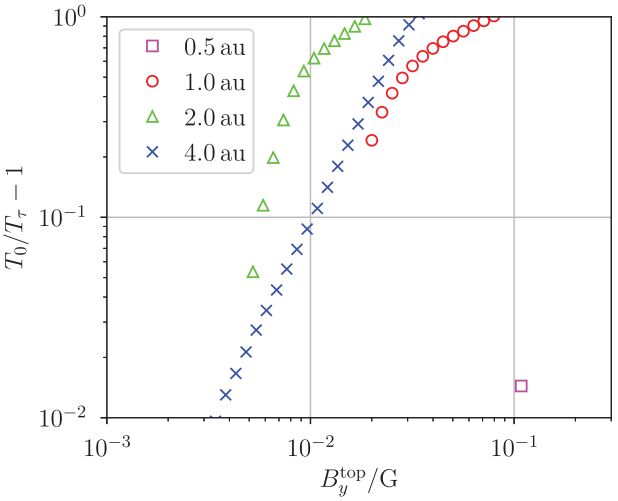

Figure 15. Temperature contrast between the mid-plane and the $\tau = 1$ altitude as a function of the surface azimuthal field $B_y^{\rm top}$ at different radii from the star (see the legend) in externally driven equilibria with $\beta = 10^5$.

4.3 Dependence on surface magnetic field

We now sample different radii r and azimuthal magnetic fields $B_y^{\rm top}$ while keeping every other parameter fixed as in Section 4.2. For each externally driven solution we compute the dimensionless dissipation coefficient α via equation (31) and represent it on Fig. 14. The magnetic field $B_y^{\rm top}$ is arbitrarily measured in Gauss units.

The dissipation coefficient α increases with $B_y^{\rm top}$ at the four radii considered. Its values range from $\alpha = 10^{-7}$ to 10^{-1} for the interval of $B_y^{\rm top}/{\rm G} \in [10^{-4}, 10^{-1}]$ considered. As mentioned in Section 4.2.1, the surface magnetic field is near equipartition with the gas pressure for $B_y^{\rm top}/{\rm G} = 2 \times 10^{-2}$ at $r = 1$ au. All the solutions presented on Fig. 14 are in this regime of moderate magnetization.

We find a roughly quadratic scaling of the dissipation coefficient α with $B_y^{\rm top}$, most apparent at low $B_y^{\rm top}$ or in the $r = 4$ au case. We also note that the graphs of the dimensional heat flux $Q_{\rm O} + Q_{\rm A}$ as a function of $B_y^{\rm top}$ (not shown) are nearly superimposed on each other, so the separation between the four solution branches on Fig. 14 mainly reflects variations of the normalization coefficient

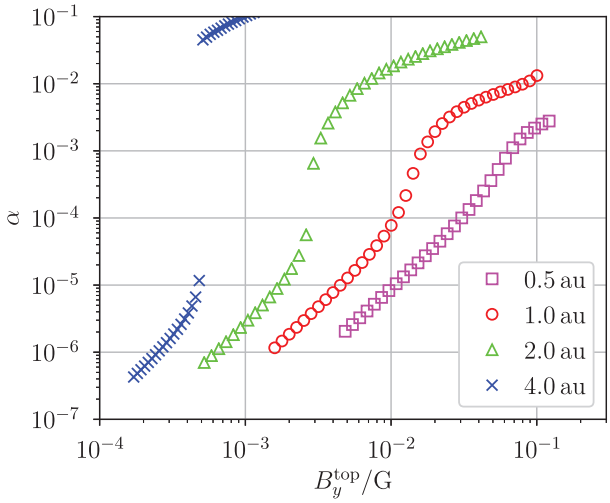

Figure 16. Same as Fig. 14 with a reversed polarity for the net magnetic field $B_z < 0$.

$\Sigma h^2 \Omega^3$ with radius. Since the energy dissipated in the disc is related to the surface energy flux $F_z^{\rm top}$ via equation (33), it does not have to scale with the characteristic energy flux of the disc $\Sigma h^2 \Omega^3$.

On Fig. 15, we show the temperature contrast $T_0/T_\tau - 1$ measured in the same series of equilibria as on Fig. 14. At $r \geq 1$ au, the temperature contrast increases from 10^{-2} to $\sim$1 over one decade in $B_y^{\rm top}$. This range of $B_y^{\rm top}$ is independent of the strength of the vertical field B_z threading the disc as long as $\beta \gg 1$ because only (B_x, B_y) can generate electric currents in this 1D model, and the net B_z only weakly contributes to the ambipolar diffusivity.

When considering the opposite polarity $B_z < 0$ for the net magnetic field, we found that the current-free equilibrium was always linearly stable and therefore supported no energy dissipation by itself. This polarity dependence is introduced by the Hall effect in the induction equation. Since the externally driven states do not rely on a linear instability as the energy source, we can freely impose an energy flux $F_z^{\rm top}$ on a disc with $B_z < 0$ and obtain different dissipation properties than in the $B_z > 0$ case.

We show on Fig. 16 the dissipation coefficient α obtained when repeating the same parameter sampling as for Fig. 14 but with the opposite polarity for the net magnetic field: $B_z < 0$. As previously, α is an increasing function of $B_y^{\rm top}$ at every radii and spans the range $[10^{-7}, 10^{-1}]$ over the interval of $B_y^{\rm top}$ considered.

The solution branches corresponding to $r = 0.5$ and 1 au are qualitatively the same as on Fig. 14. At $r = 1$ au, the dissipation coefficient α is greater than in the $B_z > 0$ case by at most a factor $\approx$4. The difference becomes more significant at $r = 2$ au: the dissipation coefficent reaches $\alpha = 10^{-2}$ for a surface $B_y^{\rm top} \approx 7 \times 10^{-3}$ G, three times smaller than in the $B_z > 0$ case. At $r = 4$ au, the solution branch already deviates from the $B_z > 0$ case for $B_y^{\rm top} \gtrsim 4 \times 10^{-4}$ G, and α becomes over a thousand times larger than in the $B_z > 0$ case for surface fields as weak as $B_y^{\rm top} \lesssim 6 \times 10^{-3}$ G.

Interestingly, the $B_z < 0$ orientation of the net magnetic field leads to larger dissipation rates for a given magnetic field $B_y^{\rm top}$ at the surface of the disc. Since the energy dissipated in the disc is equal to the energy input at the top boundary, it implies that the energy flux $F_z^{\rm top}$ is larger in norm when $B_z < 0$. Because only the Hall effect induces such a polarity dependence, we can attribute the enhanced $F_z^{\rm top}$ to the contribution of the Hall energy flux at the surface of the disc. Reciprocally, it takes a larger energy flux at the surface of the disc to maintain a given $B_y^{\rm top}$ when $B_z < 0$.

5 DISCUSSION

5.1 Caveats

5.1.1 Chemistry and radiation

We neglected the influence of dust grains and metals in the ionization model used throughout this paper. The mid-plane abundance of free electrons can decrease by several orders of magnitude depending on the dust grain properties alone (Ivlev, Akimkin & Caselli 2016). Moreover, dust grains can directly alter the electric resistivity when considered as dominant charge carriers themselves (Salmeron & Wardle 2008; Ilgner 2012; Xu & Bai 2016). Acknowledging these uncertainties, we opted for a plausible ionization model and covered the 'dead-zone' regime when artificially decreasing the ionization fraction by a factor 10^{-2} in Section 3.4 and 10^{-3} in Section 4.

Inversely, the prescribed opacity relies on $\sim 20\,\mu$m dust grains at the temperatures considered ~ 150 K. This prescription should be valid in the inner few au, while the disc is optically thick to its own thermal radiations (Chiang & Goldreich 1997; D'Alessio, Calvet & Hartmann 2001). We obtained qualitatively similar results when reducing the opacity by a factor 10 in Section 3.5, but larger magnetizations were then required to heat the mid-plane to a given temperature.

Our model does not capture the deposition of heat by stellar photons at the disc surface and its reprocessing to thermal wavelengths. By solving for the reprocessed radiation only, we exclude the temperature stratification separating the disc from the warm stellar environment (Aresu et al. 2011; Pinte et al. 2018). Solving for the deposition of heat as implemented by Flock et al. (2013) and Kolb et al. (2013) should yield the same temperature in the mid-plane as long as the disc is thick to both the incomming and reprocessed radiations. As mentioned in Section 2.1.3, the disc surface should also be better ionized above $z/h \gtrsim 4$ by stellar FUV photons (Perez-Becker & Chiang 2011) which we omitted.

5.1.2 Imposed symmetries

The assumption of axisymmetry is supported in good approximation by both local and global disc simulations including Ohmic and ambipolar diffusion in the regime relevant to protoplanetary discs (Bai & Stone 2011; Gressel et al. 2015).

For simplicity we have imposed the symmetry (20) of the disc about the mid-plane. The symmetry supported by global disc simulations incorporating all three non-ideal MHD effects can differ from equation (20) or keep evolving with radius and time (Béthune et al. 2017). In Section 3.6, we relaxed the mid-plane conditions and verified that the flow is attracted to the same equatorial symmetry for a specific set of input parameters. However, we cannot exclude that other solutions would rather bifurcate to an 'odd' mid-plane symmetry if permitted as in Lesur et al. (2014) and Mori et al. (2019).

Our most questionable assumption is that of radial locality, and its implications are twofold. On one hand, we found that electric heating and angular momentum transport strongly depend on the conditions inside the disc. Placing our local simulations back in a global disc picture, the measure of stress α could vary on au scales and induce radially inhomogeneous accretion. The resulting gas build-ups could in turn have implication on the migration of solids (Weidenschilling 1977) or the generation of vortices (Lovelace et al. 1999; Meheut, Yu & Lai 2012). The non-ideal MHD effects also affect the radial transport of magnetic flux (Guilet & Ogilvie 2013, 2014; Leung & Ogilvie 2019). Our model does not permit this redistribution of mass and magnetic flux across neighbouring annuli.

On the other hand, this 1D model excludes radially dependent waves and instabilities. The entropy profiles examined in Section 3.3.3 suggest that some equilibria might be convectively unstable in more than one dimension (Ruden et al. 1988; Kley, Papaloizou & Lin 1993; Held & Latter 2018). The strong azimuthal magnetic field could trigger the growth of oblique modes of the ambipolar-shear instability (Kunz & Balbus 2004; Kunz 2008). In principle, the azimuthal velocity profiles $\partial_z v_y \ll \Omega$ could also trigger the vertical shear instability (Urpin & Brandenburg 1998), albeit with small growth rates and saturation amplitudes in the optically thick regions considered (Nelson, Gressel & Umurhan 2013; Lin & Youdin 2015). Our solutions might therefore be unstable and evolve toward new, not necessarily stationary states in more than one dimension.

Finally, our boundary conditions prevent the removal of energy by advection ($v_z = 0$) or by the ideal MHD Poynting flux associated with torsional Alfvén waves. This Poynting flux could be used to power outflows in jet-launching discs, so the heating rates obtained in our model should be regarded as upper limits given the orbital energy extracted by the magnetic field (Casse & Ferreira 2000).

5.2 Laminar versus turbulent discs

Assuming that mass accretion occurs via laminar magnetic torques in the inner few au, our model produces a wide range of $\alpha \in [10^{-7}, 10^{-1}]$ depending on the ionization and magnetization of the disc. Values as high as $\alpha \gtrsim 10^{-2}$ would not necessarily induce measurable accretion rates since they are restricted to narrow radial ranges, favouring the formation of substructures in the disc instead.

Large values $\alpha > 10^{-4}$ are noteworthy for several reasons. First, they support the possibility of magnetically driven accretion in regions where the MRI should be resistively damped (Gammie 1996). The Hall effect plays a major role in destabilizing the disc (Balbus & Terquem 2001; Wardle & Salmeron 2012), and in producing a laminar magnetic stress as obtained in both local (Lesur et al. 2014; Bai 2015) and global simulations (Béthune et al. 2017; Bai 2017). On the other hand, should the resistivity be large enough to stabilize the disc (e.g. at lower ionization fractions), electric currents originating from large-scale accretion-ejection structures may still permeate the disc (Ferreira 1997), inducing significant heating and accretion inside $z/h \lesssim 3$.

Second, turbulent motions inferred from molecular line broadening and dust lifting seem compatible with $\alpha_{\rm SS} \sim 10^{-4}$ (Flaherty et al. 2015, 2017; Pinte et al. 2016), where $\alpha_{\rm SS}$ is the Shakura & Sunyaev (1973) measure of turbulent stress. If angular momentum was only transported by turbulence, then this $\alpha_{\rm SS}$ should match the one measured by turbulent heating and mass accretion (Balbus & Papaloizou 1999). However, if the magnetic stress is primarily laminar then the heating and mass accretion rates can be much larger than those suggested by the gas kinematics alone. While the magnetic field provides most of the stress in a laminar fashion, hydrodynamic or dust-gas instabilities may be responsible for turbulence at the observed amplitudes $\alpha_{\rm SS} \sim 10^{-4}$ (e.g. Youdin & Goodman 2005; Fromang & Lesur 2019).

5.3 Comparison with the work of Mori et al. (2019)

The closest study to ours is that of Mori et al. (2019), who concluded that electric heating should have a negligible impact on the temperature of the inner disc compared to stellar irradiation. There are a number of differences between their model and ours which hinder a direct quantitative comparisons. In particular:

(i) They deduce the thermal structure of the disc from the MHD heating rates computed in an isothermal disc. Although this method is not self-consistent, we believe that it can be a good approximation as long as the obtained temperature contrast is smaller than unity.

(ii) They consider gas opacities ranging from 5×10^{-1} to 5×10^{-3} cm^2 g^{-1}, that is 10–1000 times lower than our reference case. Their largest opacity is comparable to our reduced opacity case of Section 3.5, where we obtained consequently lower temperature contrasts. We believe that this is the main cause of discrepancy between our results and those of Mori et al. (2019). Our results support their conclusion of inefficient accretion heating in the limit of low disc opacities.

(iii) They let the disc evolve in the two-sided domain $z/h \in [-8, +8]$ and only obtain the 'odd' mid-plane symmetry discussed in Section 3.6. This symmetry supports no electric current in the disc mid-plane, whence electric heating is localized away from the mid-plane and does not favour heat accumulation inside the disc.

The method of Mori et al. (2019) might also introduce biases in the energy budget which are difficult to quantify a priori. First, to make the problem affordable in computational time they capped the magnetic diffusivities to an arbitrary ceiling value and the density to an arbitrary floor value. While these are standard and necessary procedures for common time-integration schemes, they directly alter the heating powers and indirectly affect the electric current density inside the disc. Second, their vertical boundary conditions allow the spontaneous launching of an outflow from the disc. Although outflows are a natural outcome of global magnetized disc models, they suffer from convergence issues in the local shearing box model (Fromang et al. 2013; Lesur, Ferreira & Ogilvie 2013) which might affect the energetic balance of the flow. For example, the vertical acceleration of the flow determines the importance of adiabatic cooling. Additionally, to reach a steady state the mass lost through the outflow must be artificially re-injected inside the domain, which supplies internal energy as well if the temperature is left unaltered.

6 SUMMARY

We computed the steady-state vertical structure of a circumstellar disc at radii relevant to planet formation – 0.5 to 4 au in the chosen disc model. We considered weakly ionized and weakly magnetized discs in which angular momentum transport and internal heating are laminar processes, and we precluded outflows. Simplified prescriptions for the gas opacity and ionization fraction allowed us to self-consistently model the energy exchanges in a radiative, non-ideal MHD framework. We considered two different origins for the energy dissipated in the disc, either:

(i) the energy of the Keplerian shear is extracted by internal stresses following the growth of the HSI inside the disc (labelled 'internally driven' states),

(ii) or energy is supplied at the surface of the disc through the twisting of a large-scale poloidal field ('externally driven' states).

Our results support the following conclusions:

(i) Including all three non-ideal MHD effects and a weak poloidal field $\beta > 10^4$, the isothermal and current-free equilibrium can be linearly unstable for mid-plane ionization fractions as low as 10^{-15}. The instability saturates in equilibria sustaining angular momentum transport and energy dissipation. Neglecting energetic losses through an outflow, the equivalent 'viscosity' coefficients can be as high as $\alpha \sim 10^{-3}$–10^{-2}.

(ii) In the absence of linear instability, for example at lower ionization fractions, similar levels of dissipation can occur inside the disc if the poloidal field is twisted to equipartition strength with the gas by the disc environment, as expected for global accretion-ejection structures.

(iii) The Ohmic and ambipolar resistivities transport energy vertically through the disc, allowing energy thermalization away from its original source. For a sufficiently high opacity $\kappa \gtrsim 10^{-1}$ cm^2 g^{-1}, the dissipation of electric currents driven from the disc surface can induce order unity temperature variations in the disc interior, and can in some cases lead to convective instability.

We have indications that the 1D equilibria studied in this paper should induce radial inhomogeneities in discs, and that they might be vulnerable to radially dependent perturbations. The steady state spontaneously adopted by 3D flows and the achievable level of dissipation should therefore be pursued with global MHD simulations. Because these issues depend crucially on the gas opacity and ionization fraction, realistic quantitative predictions require a detailed treatment of chemistry and radiation as it becomes computationally affordable (Xu et al. 2019; Wang et al. 2019; Thi et al. 2019).

ACKNOWLEDGEMENTS

We thank Gordon Ogilvie and Christian Rab for contextualizing externally driven solutions and flux-limited radiative transport in protoplanetary discs. We thank the anonymous reviewer for his careful reading of the paper and for the suggested corrections and clarifications. We also thank Geoffroy Lesur, Xuening Bai, and Martin Pessah for their comments on the final draft. WB gratefully acknowledges funding by the Deutsche Forschungsgemeinschaft through Grant KL 650/31-1, as well as the Isaac Newton Trust and the Department of Applied Mathematics and Theoretical Physics of the University of Cambridge where this project started.

REFERENCES

ALMA Partnership et al., 2015, ApJ, 808, L3
Andrews S. M., Williams J. P., 2007, ApJ, 659, 705
Andrews S. M. et al., 2018, ApJ, 869, L41
Aresu G., Kamp I., Meijerink R., Woitke P., Thi W. F., Spaans M., 2011, A&A, 526, A163
Bai X.-N., 2015, ApJ, 798, 84
Bai X.-N., 2017, ApJ, 845, 75
Bai X.-N., Stone J. M., 2011, ApJ, 736, 144
Balbus S. A., Hawley J. F., 1991, ApJ, 376, 214
Balbus S. A., Papaloizou J. C. B., 1999, ApJ, 521, 650
Balbus S. A., Terquem C., 2001, ApJ, 552, 235
Bell K. R., Lin D. N. C., 1994, ApJ, 427, 987
Bergin E. A., Williams J. P., 2017, in Pessah M., Gressel O., eds, Astrophysics and Space Science Library, Vol. 445, The Determination of Protoplanetary Disk Masses. Springer International Publishing, Cham, p. 1
Béthune W., Lesur G., Ferreira J., 2017, A&A, 600, A75
Bitsch B., Raymond S. N., Izidoro A., 2019, A&A, 624, A109
Brandenburg A., Zweibel E. G., 1994, ApJ, 427, L91
Casse F., Ferreira J., 2000, A&A, 353, 1115
Chiang E. I., Goldreich P., 1997, ApJ, 490, 368
Cridland A. J., Pudritz R. E., Alessi M., 2016, MNRAS, 461, 3274
Cridland A. J., Pudritz R. E., Birnstiel T., 2017, MNRAS, 465, 3865
D'Alessio P., Cantö J., Calvet N., Lizano S., 1998, ApJ, 500, 411
D'Alessio P., Calvet N., Hartmann L., 2001, ApJ, 553, 321
Desch S. J., 2004, ApJ, 608, 509

Dodson-Robinson S. E., Willacy K., Bodenheimer P., Turner N. J., Beichman C. A., 2009, Icarus, 200, 672
Dullemond C. P., 2000, A&A, 361, L17
Ferguson J. W., Alexander D. R., Allard F., Barman T., Bodnarik J. G., Hauschildt P. H., Heffner-Wong A., Tamanai A., 2005, ApJ, 623, 585
Ferreira J., 1997, A&A, 319, 340
Ferreira J., Pelletier G., 1993, A&A, 276, 625
Flaherty K. M., Hughes A. M., Rosenfeld K. A., Andrews S. M., Chiang E., Simon J. B., Kerzner S., Wilner D. J., 2015, ApJ, 813, 99
Flaherty K. M. et al., 2017, ApJ, 843, 150
Flock M., Fromang S., González M., Commerçon B., 2013, A&A, 560, A43
Fromang S., Lesur G., 2019 , in Brun A. S., Mathis S., Charbonnel C., Dubrulle B., eds, EAS Publ. Ser., Vol. 82, EDP Science, Les Ulis, France, p. 391
Fromang S., Terquem C., Balbus S. A., 2002, MNRAS, 329, 18
Fromang S., Latter H., Lesur G., Ogilvie G. I., 2013, A&A, 552, A71
Gammie C. F., 1996, ApJ, 457, 355
Goldreich P., Lynden-Bell D., 1965, MNRAS, 130, 125
Goodman J., Xu G., 1994, ApJ, 432, 213
Gressel O., Turner N. J., Nelson R. P., McNally C. P., 2015, ApJ, 801, 84
Guilet J., Ogilvie G. I., 2013, MNRAS, 430, 822
Guilet J., Ogilvie G. I., 2014, MNRAS, 441, 852
Hawley J. F., Balbus S. A., 1992, ApJ, 400, 595
Hayashi C., 1981, Prog. Theor. Phys. Suppl., 70, 35
Held L. E., Latter H. N., 2018, MNRAS, 480, 4797
Hill G. W., 1878, Am. J. Math., 1, 5
Hyodo R., Ida S., Charnoz S., 2019, A&A, 629, A90
Ida S., Lin D. N. C., 2008, ApJ, 685, 584
Igea J., Glassgold A. E., 1999, ApJ, 518, 848
Ilgner M., 2012, A&A, 538, A124
Ivlev A. V., Akimkin V. V., Caselli P., 2016, ApJ, 833, 92
Jin L., 1996, ApJ, 457, 798
Kamp I., Thi W. F., Woitke P., Rab C., Bouma S., Ménard F., 2017, A&A, 607, A41
Kley W., Papaloizou J. C. B., Lin D. N. C., 1993, ApJ, 416, 679
Kolb S. M., Stute M., Kley W., Mignone A., 2013, A&A, 559, A80
Kunz M. W., 2008, MNRAS, 385, 1494
Kunz M. W., Balbus S. A., 2004, MNRAS, 348, 355
Kunz M. W., Lesur G., 2013, MNRAS, 434, 2295
Latter H. N., Papaloizou J., 2017, MNRAS, 472, 1432
Latter H. N., Fromang S., Gressel O., 2010, MNRAS, 406, 848
Lesur G., Ferreira J., Ogilvie G. I., 2013, A&A, 550, A61
Lesur G., Kunz M. W., Fromang S., 2014, A&A, 566, A56
Leung P. K. C., Ogilvie G. I., 2019, MNRAS, 487, 5155
Lin M.-K., Youdin A. N., 2015, ApJ, 811, 17
Lorek S., Lacerda P., Blum J., 2018, A&A, 611, A18
Louvet F., Dougados C., Cabrit S., Mardones D., Ménard F., Tabone B., Pinte C., Dent W. R. F., 2018, A&A, 618, A120
Lovelace R. V. E., Li H., Colgate S. A., Nelson A. F., 1999, ApJ, 513, 805
Lovelace R. V. E., Li H., Koldoba A. V., Ustyugova G. V., Romanova M. M., 2002, ApJ, 572, 445
Lovelace R. V. E., Rothstein D. M., Bisnovatyi-Kogan G. S., 2009, ApJ, 701, 885
Meheut H., Yu C., Lai D., 2012, MNRAS, 422, 2399
Minerbo G. N., 1978, J. Quant. Spec. Radiat. Transf., 20, 541
Mori S., Bai X.-N., Okuzumi S., 2019, ApJ, 872, 98
Nelson R. P., Gressel O., Umurhan O. M., 2013, MNRAS, 435, 2610
Oya Y. et al., 2019, ApJ, 881, 112
Pelletier G., Pudritz R. E., 1992, ApJ, 394, 117
Perez-Becker D., Chiang E., 2011, ApJ, 735, 8
Pinte C., Dent W. R. F., Ménard F., Hales A., Hill T., Cortes P., de Gregorio-Monsalvo I., 2016, ApJ, 816, 25
Pinte C. et al., 2018, A&A, 609, A47
Pudritz R. E., Norman C. A., 1983, ApJ, 274, 677
Riols A., Ogilvie G. I., Latter H., Ross J. P., 2016, MNRAS, 463, 3096
Rodenkirch P. J., Klahr H., Fendt C., Dullemond C. P., 2020, A&A, 633, A21
Ruden S. P., Papaloizou J. C. B., Lin D. N. C., 1988, ApJ, 329, 739
Safier P. N., 1993, ApJ, 408, 115
Salmeron R., Wardle M., 2008, MNRAS, 388, 1223
Sano T., Miyama S. M., Umebayashi T., Nakano T., 2000, ApJ, 543, 486
Shakura N. I., Sunyaev R. A., 1973, A&A, 500, 33
Suriano S. S., Li Z.-Y., Krasnopolsky R., Shang H., 2018, MNRAS, 477, 1239
Tazzari M. et al., 2017, A&A, 606, A88
Thi W. F., Lesur G., Woitke P., Kamp I., Rab C., Carmona A., 2019, A&A, 632, A44
Umebayashi T., Nakano T., 1981, PASJ, 33, 617
Umebayashi T., Nakano T., 2009, ApJ, 690, 69
Urpin V. A., 1984, SvA, 28, 50
Urpin V., Brandenburg A., 1998, MNRAS, 294, 399
Walsh C., Nomura H., van Dishoeck E., 2015, A&A, 582, A88
Wang L., Bai X.-N., Goodman J., 2019, ApJ, 874, 90
Wardle M., 1999, MNRAS, 307, 849
Wardle M., 2007, Ap&SS, 311, 35
Wardle M., Salmeron R., 2012, MNRAS, 422, 2737
Weidenschilling S. J., 1977, MNRAS, 180, 57
Weingartner J. C., Draine B. T., 2001, ApJ, 563, 842
Xu R., Bai X.-N., 2016, ApJ, 819, 68
Xu R., Bai X.-N., Öberg K., Zhang H., 2019, ApJ, 872, 107
Youdin A. N., Goodman J., 2005, ApJ, 620, 459

APPENDIX A: ALTERNATIVE EXAMPLE SOLUTION

We draw on Fig. A1 the vertical profiles of an equilibrium with $\beta = 10^6$ at a radius of $r = 1$ au. It is twice closer to the star than

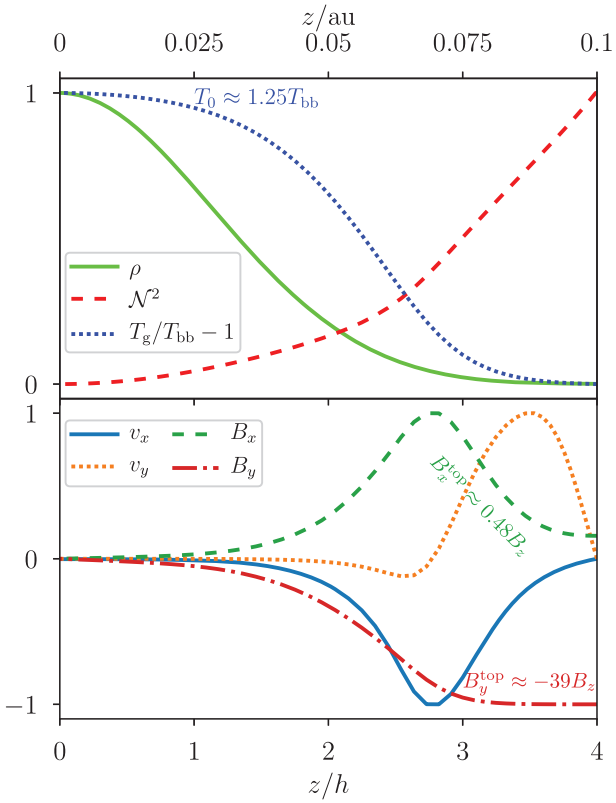

Figure A1. Vertical profiles of the flow variables in an equilibrium with $\beta = 10^6$ at $r = 1$ au, normalized by their extremal value for visibility. Upper panel: density (solid green), squared Brünt–Väisälä frequency (dashed red), and gas temperature relative to $T_{\rm bb}$ (dotted blue). Lower panel: radial velocity (solid blue), azimuthal velocity (dotted orange), radial magnetic field (dashed green), and azimuthal magnetic field (dotted–dashed red).

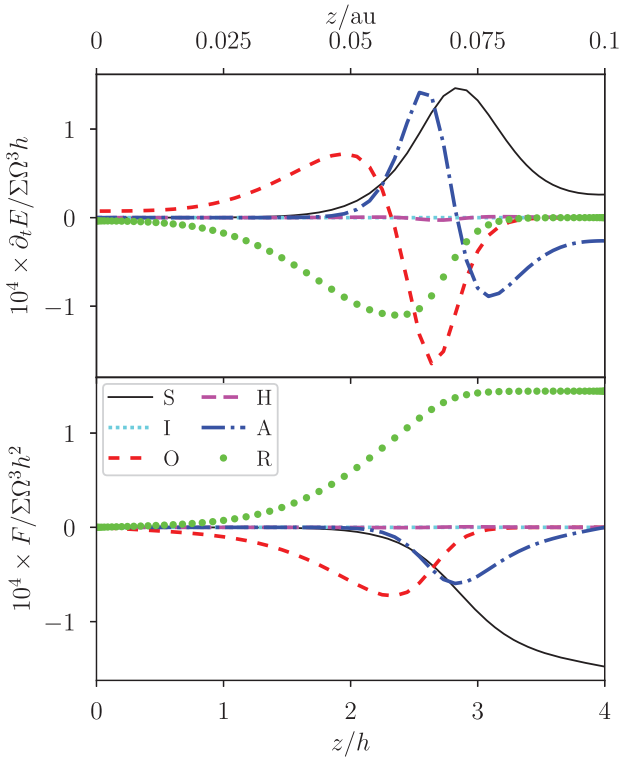

Figure A2. Energy budget in the same equilibrium as on Fig. A1. Upper panel: total energy equation (27). Lower panel: associated energy fluxes, equivalent to the vertical integral of equation (27) from the mid-plane. the different curves correspond to the source term ('S', solid black), the ideal induction ('I', dotted cyan), Ohmic resistivity ('O', dashed red), the Hall drift ('H', dashed magenta), ambipolar diffusion ('A', dot-dashed blue), and radiation ('R', green dots).

the reference equilibrium of Section 3.2, in a region where the disc is denser and the ionization fraction is lower (see Fig. 1). It is threaded by a stronger B_z to reach a comparable temperature contrast.

The gas temperature is maximal in the mid-plane with $T_0 \approx 1.25 T_{\rm bb}$, smaller than the reference case shown on Fig. 3. The squared Brünt–Väisälä frequency is also positive everywhere but overall greater than in the reference case, putting this equilibrium further away from convective instability. The velocity and magnetic fields have small amplitudes near the mid-plane and large amplitudes above $z/h \gtrsim 2$. The azimuthal component of the magnetic field reaches $B_y^{\rm top} \approx -39 B_z$ at the disc surface, about three times weaker then in the reference case.

We decompose the energy equation (27) for this equilibrium on Fig. A2. The source term, related to the extraction of orbital energy via the xy stress, is maximal at $z/h \approx 2.8 \pm 0.5$ and essentially zero below $z \lesssim h$. The absence of stress in the mid-plane indicates that this region is linearly stable to vertical perturbations on a scale $\sim h$. The energy extracted from the shear is transported downward by ambipolar diffusion and then by Ohmic diffusion. The orbital energy can thus be thermalized away from the 'active' surface layers which support most of the stress. Even if electric heating predominantly happens above $z/h \gtrsim 1$, this heat accumulates in the mid-plane for optically thick discs as expressed by equation (35) in Section 4.2.2.

APPENDIX B: TEST OF THE IMPLICIT INTEGRATOR

We verify that our numerical scheme properly captures the physics of the problem by simulating the growth of the HSI in a stratified, weakly ionized, and isothermal disc. For simplicity, we do not include the pressure and radiation equations, and we compute the MHD diffusivities $\eta_{\rm O,\,H,\,A}$ assuming a constant ionization fraction $x_e = 10^{-12}$. We initialize the disc in a current-free equilibrium (19) with $\beta = 10^6$ and $P = \rho c_s^2$ at all times and altitudes. We add a noise of small amplitude 10^{-6} on top of this equilibrium to seed the instability. We keep the damping term $\Omega h^2 \partial_z^2 v_z$ in equation (13) for consistency with the rest of the paper; this term does not affect the linear phase of the instability for which $v_z = 0$.

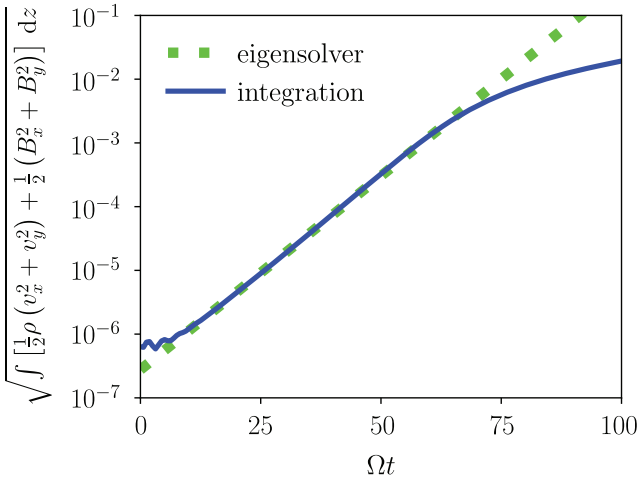

Figure B1. Square root of the vertically integrated energy perturbation when starting from the current-free equilibrium with $\beta = 10^6$ and a constant ionization fraction $x_e = 10^{-12}$. The solid blue curve corresponds to the first-order implicit integration; and the dotted green line indicates the predicted growth rate $1.40 \times 10^{-1}\Omega$ of the fastest growing eigenmode.

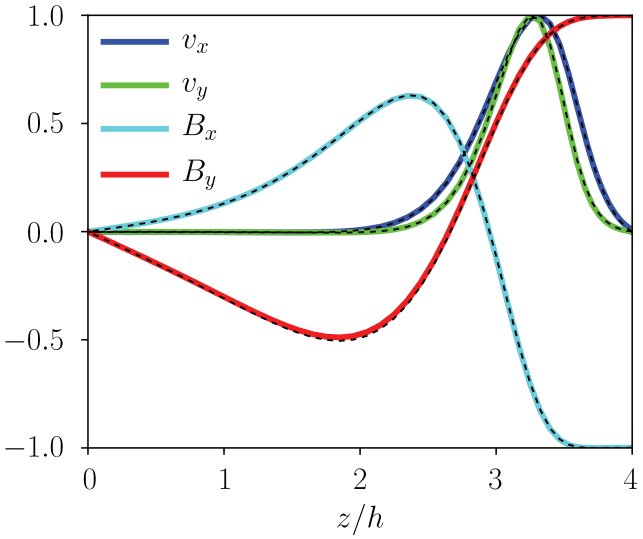

Figure B2. Vertical structure of the unstable mode growing in the implicit integration test. The thick solid curves represent the instantaneous profiles at $\Omega t = 35$; and the thin dashed curves represent the eigenmode with growth rate $1.40 \times 10^{-1}\Omega$ predicted by linear analysis. The curves have been normalized to fit in the range $[-1, 1]$.

Separately, we linearize the system of equations (3)–(5) about the current-free equilibrium (19) assuming an isothermal equation of state $P = \rho c_s^2$. We obtain the set of tangent eigenvalues and eigenmodes numerically. For the equilibrium considered, there are two unstable eigenmodes with associated eigenvalues (growth rates) 2.76×10^{-2} and $1.40 \times 10^{-1}\,\Omega$. Starting from the perturbed equilibrium, the fastest growing mode should quickly dominate the vertical structure of the flow.

Fig. B1 shows how the amplitude of the perturbations grows in time. The exponential growth appears after $\Omega t \gtrsim 8$. The growth rate obtained by first-order implicit integration matches the predicted growth rate $1.40 \times 10^{-1}\,\Omega$ to per cent accuracy during this phase. The growth of the perturbations slows down after $\Omega t \gtrsim 60$, marking the non-linear saturation of the instability.

Fig. B2 shows the vertical structure of the flow at $\Omega t = 35$, that is during the exponential growth phase. The vertical profiles of velocity and magnetic field match those of the fastest growing eigenmode over the whole extent of the computational domain, confirming that the instability is accurately resolved in space.

APPENDIX C: CONVERGENCE WITH DOMAIN SIZE

Throughout this paper, we fixed the vertical extent of the domain to $L_z = 4h$ so as to focus our resolution near the mid-plane while including most of the mass and electric current passing through the disc. The gas inside the computational domain is causally connected to the boundaries, so the upper boundary conditions necessarily affect the structure of the steady-state solutions. In particular, imposing $\partial_z B_y = 0$ at a finite height might truncate the electric current distribution and lead to underestimated heat fluxes Q. We now examine the convergence rate of the heat flux with domain size L_z.

We vary L_z from 3 to $4.5h$ in internally driven equilibria with $\beta = 10^6$ at $r = 1$ au. The case $L_z = 4h$ corresponds to the equilibrium shown on Fig. A1. Larger domain sizes $L_z > 4.5$ place severe constraints on the numerical stability of the integration scheme when including radiation transport, presumably due to the short radiative time-scales of the uppermost layers. Since the energy source is maximal away from the mid-plane for this choice of r and β ($z/h \approx 2.8 \pm 1$, cf. upper panel of Fig. A2), this equilibrium should be a defavourable case regarding convergence rates.

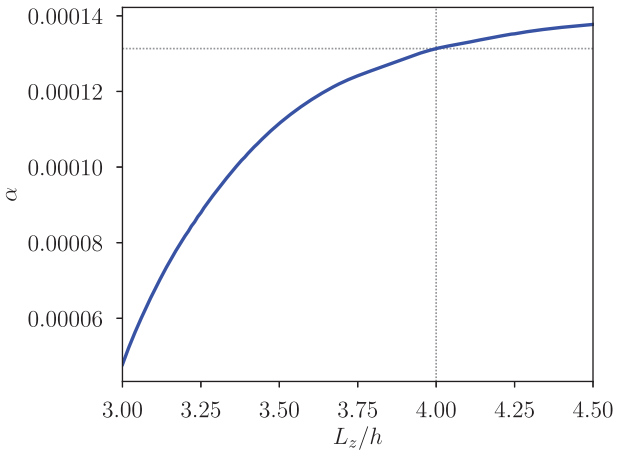

Figure C1. Dissipation coefficient α as a function of the box size L_z for internally driven equilibria with $\beta = 10^6$ at $r = 1$ au. The dotted lines indicate our standard value for the box size $L_z/h = 4$ and the corresponding α as marked on Fig. 6.

Fig. C1 shows that the dissipation coefficient α increases with L_z, supporting the idea that the heat flux Q is underestimated when truncating the domain at a finite height. The heat flux increases mostly below $L_z/h \lesssim 3.5$, corresponding to the range of altitude where energy is extracted from the Keplerian shear by the xy stress, see Fig. A2. For $L_z/h \gtrsim 4$, the heat flux keeps slowly increasing with L_z, also in agreement with the non-vanishing stress above the disc. Considering the slow convergence rate of α with L_z, the dissipation coefficients presented throughout this paper should be placed within 10 per cent confidence intervals regarding the sensitivity to the domain size L_z.

Our model does not account for the transition from the disc to the stellar environment. A sharp thermochemical transition may be induced by stellar X and FUV photons (Aresu et al. 2011; Perez-Becker & Chiang 2011) at altitudes of roughly $z/h \gtrsim 4$, with implications on the ionization fraction and the launching of outflows. Since this transition would affect the plasma conductivity and its energetics, simply extending our 1D disc model to larger domains $L_z \gtrsim 4h$ would not yield more realistic results.

This paper has been typeset from a TEX/LATEX file prepared by the author.